Journal of
Mechanics of
Materials and Structures

COMPUTATIONAL SHELL MECHANICS BY HELICOIDAL MODELING
II: SHELL ELEMENT

Teodoro Merlini and Marco Morandini

msp

COMPUTATIONAL SHELL MECHANICS BY HELICOIDAL MODELING II: SHELL ELEMENT

TEODORO MERLINI AND MARCO MORANDINI

The virtual work of stresses developed in Part I for the helicoidal shell model and then reduced to the material surface is taken as one term of a variational principle stated on a two-dimensional domain. The other terms related to the external loads and to the boundary constraints are added here and include a weak-form treatment of the constraints, which becomes necessary in the context of helicoidal modeling. All terms are cast in incremental form and yield a linearized variational principle of the virtual work type for two-dimensional continua, endowed with an internal constraint conjugate to an extra stress field that is able to control the drilling degree of freedom.

The virtual functional and the virtual tangent functional are approximated by the finite element method, using helicoidal interpolation for the kinematic field (which ensures objectivity and path independence) and a uniform representation for the extra stress field. A low-order four-node shell element is obtained, with 6 degrees of freedom per node and a unique stress-vector discrete unknown per element. Several test cases demonstrate the performance of the element and its outstanding locking-free behavior.

1. Introduction

This second part of the paper deals with the finite element approximation of the mechanics of the shell material surface, whose kinematical description was introduced in Part I. The formulation, which is briefly outlined here, follows a straightforward course. The intrinsic mechanics of the material surface are stated directly from a variational approach. The virtual work of stresses was developed in Part I for the helicoidal shell model and then reduced to the material surface; here, the external loads and the boundary constraints are introduced, and the proposed variational principle is stated on a two-dimensional domain. This principle is of the virtual work type for nonpolar continua and is endowed with an internal constraint related to an extra stress field; it also includes a weak-form treatment of the boundary constraints. The variational principle is given an incremental form from the beginning and exploits the shell linearized constitutive law obtained in Part I; then, the virtual functional and the virtual tangent functional are approximated by the finite element method.

Within the formulation outlined above, the two characteristic features of the present contribution, already introduced in Part I, are still in evidence. As with the three-dimensional mechanics, the material surface mechanics are based on a micropolar description. Since the shell is essentially nonpolar in its tangent plane, this description entails a workless stress parameter whose role is to force the definition of the drilling degree of freedom. Even if this workless stress parameter cannot be identified as the axial vector of a stress tensor, nevertheless an extra stress exists and is rightly introduced as one of the

parameters that control the Biot-axial distribution within the shell model thickness. This vector parameter is an irreducible primary unknown of the intrinsic shell mechanics: in the proposed finite element scheme (4 nodes by 6 DOFs), a unique extra stress vector per element (3 stress components) is sufficient to control the drilling rotation ensuing from a three-parametric representation of the nodal rotations.

The second characteristic feature is of great importance in Part II as well. As explained in Part I, Section 3, an integral kinematic field that couples displacements and rotations is adopted for the material surface. In this paper, helicoidal modeling is fully exploited to define the approximate kinematic field within the shell element. The local orientoposition and curvatures are computed from the nodal oriento-positions by means of a new kind of multiplicative interpolation proposed by [Merlini and Morandini 2004b]. This methodology is endowed with the important properties of objectivity and path independence and allows us to build curved and curving elements based on nodal frames and capable of large displacements and rotations. In such elements, the nodal orientations control both the orientation and the position of the material surface at any internal point. This is clearly evident from Figure 1, where the striking difference between two interpolation schemes — the classical and the helicoidal — is shown on a quadrilateral element.

In the last two decades a considerable number of high-performing shell elements have been developed. Some elements are built on mixed or full three-field variational formulations [Sansour and Bufler 1992; Wagner and Gruttmann 2005; Klinkel et al. 2008]. Other elements (for example, [Chróścielewski et al. 1992; Arciniega and Reddy 2007]) rely on high-order interpolants in order to avoid, or mitigate, shear and membrane locking. Others are based on particular techniques, such as reduced integration [Wriggers and Gruttmann 1993; Hauptmann et al. 2000; Cardoso and Yoon 2005], discrete Kirchhoff–Love constraints [Areias et al. 2005], or incompatible modes [Ibrahimbegović and Frey 1994]. Most of the elements proposed in the literature, however, use the assumed natural strain or enhanced assumed strain concepts, such as those developed by [Büchter et al. 1994; Bischoff and Ramm 1997; Sansour and Kollmann 2000; Fontes Valente et al. 2003; Chróścielewski and Witkowski 2006; Brank 2008], to mention just a few. Few are the successful low-order displacement-based elements free of any of the above techniques; see, for example, [Campello et al. 2003; Pimenta et al. 2004]. The element proposed in the present paper is based on an alternative modeling of the continuum and does not rely on any of the above-mentioned techniques. Here, the intrinsic coupling between positions and orientations proves to be the key for the successful development of a low-order four-node element that is essentially free from membrane and shear locking.
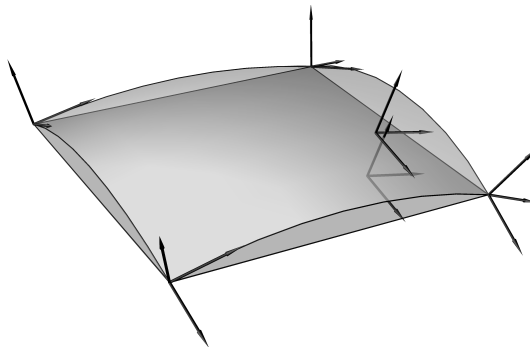
Figure 1. A curved helicoidal shell element over a classical flat element.

In a sense, the present element can be thought of as a high-order element, because helicoidal modeling allows us to describe curved and curving surfaces in a natural way despite low-order interpolants. The locking-free behavior of the element has to be likely ascribed to a fair approximate representation of the orientoposition field, faithful to the helicoidal modeling of the surface: the proposed coupling of positions and orientations of the interpolated field strictly reflects the coupling inherent in helicoidal modeling (Part I, Section 2.2).

This paper also has to tackle another problem that arises when the evolution of the discrete model along the solution process (that is, the rototranslation of the nodal frames) is described through incremental helicoidal motions. The problem is that of selective external constraints, that is, when nodes — or, in general, structure boundaries — are constrained along some degrees while the remaining degrees keep free. Selective constraints are hardly consistent with helicoidal motion: partial constraints on some components of incremental helices are unlikely in common practice. In our past computations, we could fulfill selective constraints by grounding appropriate incremental unknowns along a self-based solution process [Merlini and Morandini 2005]. This expedient, however, cannot be used with every problem: the hemispherical shell test case, for instance, when modeled as a quarter of the dome, requires selective symmetry constraints that cannot be handled by simply grounding appropriate incremental unknowns. Therefore, a nonlinear constraint element, capable of dealing with external constraints in weak form, has been developed.

The paper is organized as follows. The formulation of the variational principle, including the treatment of external loads and selective constraints, is discussed and linearized in Section 2. In Section 3, the interpolations are introduced and the linearized variational principle is approximated by the finite element method. In Section 4, several numerical examples are presented to demonstrate the performance of the proposed element. Section 5 concludes the paper.

2. Material surface variational mechanics

As stated in Part I, the starting point for the present formulation in shell mechanics is the principle of virtual work. It can be written in the form $\Pi_{\text{int}\delta} + \Pi_{\text{ext}\delta} + \Pi_{\text{bc}\delta} = 0$, where the contributions to the virtual functional from the stresses, the external loads and the boundary constraints are kept separate. The term $\Pi_{\text{int}\delta}$ was introduced in Part I, Equation (35) and developed and linearized therein assuming the helicoidal shell model for the reduction from three dimensions. In this section, the terms $\Pi_{\text{ext}\delta}$ and $\Pi_{\text{bc}\delta}$ are discussed directly for the two-dimensional material surface, and are consistently linearized.

2.1. *Virtual functionals*. The contributions from the external loads and boundary constraints are taken from the analogous terms written for the three-dimensional formulation based on helicoidal modeling [Merlini and Morandini 2004a]. For the shell material surface, they can be cast in the form (see details in [Merlini 2008b])

$$\Pi_{\text{ext}\delta} = -\int_S \langle \boldsymbol{\eta}_\delta, \boldsymbol{b} \rangle \, \mathrm{d}S - \int_{L_{\text{f}}} \langle \boldsymbol{\eta}_\delta, \boldsymbol{s} \rangle \, \mathrm{d}L_{\text{f}}, \quad \Pi_{\text{bc}\delta} = -\int_{L_{\text{c}}} \delta \langle \boldsymbol{\Lambda}^{\mathrm{T}} \boldsymbol{s}_{\text{c}}, \boldsymbol{\eta} - \boldsymbol{\eta}_{\text{c}} \rangle \, \mathrm{d}L_{\text{c}}. \tag{1}$$

Here, S is the shell surface in the reference configuration and $L = L_{\text{f}} \cup L_{\text{c}}$ its boundary line, split into free portion L_{f} and constrained portion L_{c}. The dual vectors $\boldsymbol{b} = \boldsymbol{X}'(\boldsymbol{f} + \varepsilon \boldsymbol{c}) = \boldsymbol{f} + \varepsilon(\boldsymbol{c} + \boldsymbol{x}' \times \boldsymbol{f})$ and $\boldsymbol{s} = \boldsymbol{X}'(\boldsymbol{t} + \varepsilon \boldsymbol{m}) = \boldsymbol{t} + \varepsilon(\boldsymbol{m} + \boldsymbol{x}' \times \boldsymbol{t})$ are the pole-based external load dual densities per unit reference

surface and boundary line, respectively ($X' = I + \varepsilon x' \times$ is the current position dual tensor and x' the current position vector); the relevant self-based densities, $X'^{\mathrm{T}} b = f + \varepsilon c$ and $X'^{\mathrm{T}} s = t + \varepsilon m$, are composed of the forces f and t and the couples c and m; all such load densities are valued in the current configuration; the multiplier η_δ is a virtual helix. The boundary constraint equation to fulfill in weak form is $\eta = \eta_c$, with η the helix of the unknown rototranslation $H = A'A^{\mathrm{T}}$ and η_c a known dual vector; $s_c = X'(t_c + \varepsilon m_c) = t_c + \varepsilon(m_c + x' \times t_c)$ is the pole-based unknown reaction dual density on L_c, and $t_c + \varepsilon m_c$ is the relevant self-based version, with t_c the traction and m_c the couple.

Equation (1)$_2$ shows that the constraint virtual functional $\Pi_{\mathrm{bc}\delta}$ is actually the virtual variation of a finite functional. Recalling the differential map of the rototranslation, $\eta_\delta = \Lambda \delta \eta$ (Part I, Equation (7)), the constraint virtual functional can be developed as $\Pi_{\mathrm{bc}\delta} = -\int_{L_c} \langle \eta_\delta, s_c \rangle \, dL_c - \int_{L_c} \langle \delta(\Lambda^{\mathrm{T}} s_c), \eta - \eta_c \rangle \, dL_c$. The first term is the virtual work of the constraint reactions, and the second term represents the weak form of the constraint condition. The account of the virtual multiplier in the second term was given in [Merlini and Morandini 2004a] for three-dimensional elasticity, and rewritten for material surface mechanics in [Merlini 2008b].

So far, the constraint condition of a boundary particle is cast in terms of rototranslation. However, such kinds of constraints (say, helicoidal constraints) are hardly of interest in common practice, since the single six components of a dual helix $\eta = \varphi + \varepsilon \rho$, and in particular the components of its linear part ρ, lose in general physical significance in real applications. In fact, it is difficult just to devise the assignment of a nonnull constraint η_c. Furthermore, difficulties arise in the case of *selective constraints*, when a boundary particle has some directions constrained and others free [Merlini and Morandini 2004a]. A convenient way of tackling the issue of selective constraints is to write them with a variational formulation based on classical Euclidean-rotational modeling, then to rephrase them in the context of helicoidal modeling. A constraint variational formulation of this kind was developed, linearized, and applied to helicoidal modeling by [Merlini 2008a], with reference to three-dimensional elasticity. The same formulation can be rewritten for the material surface starting from the constraint virtual functional

$$\Pi_{\mathrm{bc}\delta} = -\int_{L_c} \delta(\langle t_c, u - u_c \rangle + \langle \Gamma^{\mathrm{T}} m_c, \varphi - \varphi_c \rangle) \, dL_c, \tag{2}$$

where u are displacements and φ rotation vectors; Γ is the mapping tensor of the differential map of the rotation Φ, such that $\varphi_\delta = \Gamma \delta \varphi$ (Part I, Equation (6)). The uncoupled structure of the linear and angular constraint conditions in (2) is straightforward. Using this expression of the constraint virtual functional instead of (1)$_2$ makes the treatment of selective constraints affordable.

A further improvement for the treatment of selective constraints is the introduction of local constraint frames. A *constraint frame* is made of three orthonormal vectors $n_j \equiv n^j$ that compose the orientation tensor $N = N^{-\mathrm{T}} = n_j \otimes i^j = n^j \otimes i_j$; this is a given tensor and is used to define the service vectors

$$\check{u}_c = N^{\mathrm{T}} u_c, \quad \check{\varphi}_c = N^{\mathrm{T}} \varphi_c, \tag{3}$$

and

$$\check{t}_c = N^{\mathrm{T}} t_c, \quad \check{m}_c = N^{\mathrm{T}} m_c. \tag{4}$$

Vectors $\check{u}_c$ and $\check{\varphi}_c$ are the known constraint displacement and rotation vector back-rotated by N^{T}, whereas $\check{t}_c$ and $\check{m}_c$ are the unknown constraint reaction and reaction couple back-rotated by N^{T}. So, the absolute components of such service vectors are just the components of the true vectors in the local constraint

frame. This fact makes it easy to apply the constraints along a subset of the boundary particle degrees of freedom, without depriving the formulation of its clean vectorial notation: in practice, it corresponds to referring the constraint to a local reference frame. Using (3) and (4), (2) is rewritten as

$$\Pi_{\text{bc}\delta} = -\int_{L_c} \delta(\langle \check{t}_c, N^T u - \check{u}_c \rangle + \langle N^T \Gamma^T N \check{m}_c, N^T \varphi - \check{\varphi}_c \rangle) \mathrm{d}L_c. \tag{5}$$

2.2. Linearization. Linearization of functional $\Pi_{\text{ext}\delta}$ is accomplished under the hypothesis of only two kinds of external loads: *dead-loads* $f_D + \varepsilon c_D$ and $t_D + \varepsilon m_D$ and *follower-loads* $\Phi(f_F + \varepsilon c_F)$ and $\Phi(t_F + \varepsilon m_F)$, with f_D, c_D, t_D, m_D and f_F, c_F, t_F, m_F assigned densities. So, the expressions of the pole-based loads in $(1)_1$ become

$$b = X'\big((f_D + \Phi f_F) + \varepsilon(c_D + \Phi c_F)\big), \quad s = X'\big((t_D + \Phi t_F) + \varepsilon(m_D + \Phi m_F)\big).$$

After realizing that $\partial(X'^T \eta_\delta) = X'^T \eta_{\partial\delta} + \frac{1}{2} \varphi_\partial \times \varphi_\delta + \frac{1}{2} \varphi_\partial \times X'^T \eta_\delta + \frac{1}{2} \varphi_\delta \times X'^T \eta_\partial$, linearization of $(1)_1$ involves simple algebraic manipulations (see [Merlini 2008b]) and yields

$$\Pi_{\text{ext}\delta} = -\int_S \{\eta_\delta\}^T \cdot \{R_{f\eta}^S\} \mathrm{d}S - \int_{L_f} \{\eta_\delta\}^T \cdot \{R_{f\eta}^L\} \mathrm{d}L_f,$$

$$\partial\Pi_{\text{ext}\delta} = -\int_S (\{\eta_\delta\}^T \cdot [D_{f\eta\eta}^S] \cdot \{\eta_\partial\} + \{\eta_{\partial\delta}\}^T \cdot \{R_{f\eta}^S\}) \mathrm{d}S - \int_{L_f} (\{\eta_\delta\}^T \cdot [D_{f\eta\eta}^L] \cdot \{\eta_\partial\} + \{\eta_{\partial\delta}\}^T \cdot \{R_{f\eta}^L\}) \mathrm{d}L_f, \tag{6}$$

where

$$\{R_{f\eta}^S\} = \begin{Bmatrix} (c_D + \Phi c_F) + x' \times (f_D + \Phi f_F) \\ f_D + \Phi f_F \end{Bmatrix},$$

$$[D_{f\eta\eta}^S] = \begin{bmatrix} \frac{1}{2}(c_D + \Phi c_F) \times + \frac{1}{2}\big(x' \times (f_D + \Phi f_F) \times + (f_D + \Phi f_F) \times x' \times\big) & \frac{1}{2}(f_D + \Phi f_F) \times^T \\ \frac{1}{2}(f_D + \Phi f_F) \times & 0 \end{bmatrix}$$
$$- \begin{bmatrix} (\Phi c_F) \times + x' \times (\Phi f_F) \times & 0 \\ (\Phi f_F) \times & 0 \end{bmatrix},$$

and

$$\{R_{f\eta}^L\} = \begin{Bmatrix} (m_D + \Phi m_F) + x' \times (t_D + \Phi t_F) \\ t_D + \Phi t_F \end{Bmatrix},$$

$$[D_{f\eta\eta}^L] = \begin{bmatrix} \frac{1}{2}(m_D + \Phi m_F) \times + \frac{1}{2}\big(x' \times (t_D + \Phi t_F) \times + (t_D + \Phi t_F) \times x' \times\big) & \frac{1}{2}(t_D + \Phi t_F) \times^T \\ \frac{1}{2}(t_D + \Phi t_F) \times & 0 \end{bmatrix}$$
$$- \begin{bmatrix} (\Phi m_F) \times + x' \times (\Phi t_F) \times & 0 \\ (\Phi t_F) \times & 0 \end{bmatrix}.$$

As assumed in Part I, here and in the following the sequence angular–linear is understood while writing dual vectors and tensors in matrix notation. So, for example, in column $\{\eta_\delta\}$ vector φ_δ is the first element and vector ρ_δ the second.

Linearization of the functional $\Pi_{\text{bc}\delta}$ needs more skills about the successive differentiations of the rotation tensor [Merlini 2002; 2003]. Here, it suffices to recall that $\partial\varphi_\delta = \varphi_{\partial\delta} + \frac{1}{2}\varphi_\partial \times \varphi_\delta$, $\varphi_\delta = \Gamma \delta\varphi$, $\delta\Gamma = \Gamma_{/} : \delta\varphi \otimes I$, $\partial\Gamma_{/} = \Gamma_{/\!/}^{1234} : \partial\varphi \otimes I$; the expressions for tensors Γ, $\Gamma_{/}$ and $\Gamma_{/\!/}^{1234}$ can be found

in [Merlini and Morandini 2004b, Appendix A]. After some algebraic manipulation [Merlini 2008b], linearization of (5) yields

$$
\Pi_{bc\delta} = -\int_{L_c}\left(\left\{\begin{matrix}\boldsymbol{\varphi}_\delta\\ \delta\boldsymbol{u}\end{matrix}\right\}^{\mathrm{T}}\cdot\left\{\begin{matrix}\boldsymbol{Q}_{\mathrm{IIc}}\check{\boldsymbol{m}}_c\\ N\check{\boldsymbol{t}}_c\end{matrix}\right\} + \left\{\begin{matrix}\delta\check{\boldsymbol{m}}_c\\ \delta\check{\boldsymbol{t}}_c\end{matrix}\right\}^{\mathrm{T}}\cdot\left\{\begin{matrix}\boldsymbol{Q}_{\mathrm{Ic}}\\ \boldsymbol{Q}_{\mathrm{Lc}}\end{matrix}\right\}\right)\mathrm{d}L_c,
$$

$$
\begin{aligned}
\partial\Pi_{bc\delta} = -\int_{L_c}\Bigg(&\boldsymbol{\varphi}_\delta\cdot\left[\boldsymbol{\Gamma}^{-\mathrm{T}}(\check{\boldsymbol{m}}_c\cdot\boldsymbol{Q}_{\mathrm{IIIc}})\boldsymbol{\Gamma}^{-1} + \tfrac{1}{2}(\boldsymbol{Q}_{\mathrm{IIc}}\check{\boldsymbol{m}}_c)\times\right]\cdot\boldsymbol{\varphi}_\partial + \left\{\begin{matrix}\boldsymbol{\varphi}_\delta\\ \delta\boldsymbol{u}\end{matrix}\right\}^{\mathrm{T}}\cdot\left[\begin{matrix}\boldsymbol{Q}_{\mathrm{IIc}} & \mathbf{0}\\ \mathbf{0} & N\end{matrix}\right]\cdot\left\{\begin{matrix}\partial\check{\boldsymbol{m}}_c\\ \partial\check{\boldsymbol{t}}_c\end{matrix}\right\}\\
&+\left\{\begin{matrix}\delta\check{\boldsymbol{m}}_c\\ \delta\check{\boldsymbol{t}}_c\end{matrix}\right\}^{\mathrm{T}}\cdot\left[\begin{matrix}\boldsymbol{Q}_{\mathrm{IIc}}^{\mathrm{T}} & \mathbf{0}\\ \mathbf{0} & N^{\mathrm{T}}\end{matrix}\right]\cdot\left\{\begin{matrix}\boldsymbol{\varphi}_\partial\\ \partial\boldsymbol{u}\end{matrix}\right\} + \left\{\begin{matrix}\boldsymbol{\varphi}_{\partial\delta}\\ \partial\delta\boldsymbol{u}\end{matrix}\right\}^{\mathrm{T}}\cdot\left\{\begin{matrix}\boldsymbol{Q}_{\mathrm{IIc}}\check{\boldsymbol{m}}_c\\ N\check{\boldsymbol{t}}_c\end{matrix}\right\} + \left\{\begin{matrix}\partial\delta\check{\boldsymbol{m}}_c\\ \partial\delta\check{\boldsymbol{t}}_c\end{matrix}\right\}^{\mathrm{T}}\cdot\left\{\begin{matrix}\boldsymbol{Q}_{\mathrm{Ic}}\\ \boldsymbol{Q}_{\mathrm{Lc}}\end{matrix}\right\}\Bigg)\mathrm{d}L_c,
\end{aligned}
\tag{7}
$$

where convenient tensors have been introduced as

$$
\begin{aligned}
\boldsymbol{Q}_{\mathrm{Lc}} &= N^{\mathrm{T}}\boldsymbol{u} - \check{\boldsymbol{u}}_c,\\
\boldsymbol{Q}_{\mathrm{Ic}} &= N^{\mathrm{T}}\boldsymbol{\Gamma} N(N^{\mathrm{T}}\boldsymbol{\varphi} - \check{\boldsymbol{\varphi}}_c),\\
\boldsymbol{Q}_{\mathrm{IIc}} &= N + \boldsymbol{\Gamma}^{-\mathrm{T}}\big(N^{\mathrm{T}}\boldsymbol{\Gamma}_{/}N(N^{\mathrm{T}}\boldsymbol{\varphi} - \check{\boldsymbol{\varphi}}_c)\big)^{\mathrm{T}},\\
\boldsymbol{Q}_{\mathrm{IIIc}} &= N^{\mathrm{T}}\boldsymbol{\Gamma}_{/} + N^{\mathrm{T}}\big(\boldsymbol{\Gamma}_{//}^{\underline{1234}} - (\boldsymbol{\Gamma}_{/}^{\mathrm{T}132}\boldsymbol{\Gamma}^{-1}\boldsymbol{\Gamma}_{/}^{\mathrm{T}132})^{\mathrm{T}1342}\big)N(N^{\mathrm{T}}\boldsymbol{\varphi} - \check{\boldsymbol{\varphi}}_c).
\end{aligned}
$$

In order to use the constraint virtual functionals $\Pi_{bc\delta}$ and $\partial\Pi_{bc\delta}$ in the context of helicoidal modeling, it remains to pass from Euclidean-rotational kinematics to helicoidal kinematics. The constraint reactions are conveniently grouped into the dual reaction $\check{\boldsymbol{r}}_c = \check{\boldsymbol{t}}_c + \varepsilon\check{\boldsymbol{m}}_c$ and the kinematical variables into the dual vector $\boldsymbol{e} = \boldsymbol{\varphi} + \varepsilon\boldsymbol{u}$. Consistently, the dual kinematical variation variables $\boldsymbol{e}_\delta = \boldsymbol{\varphi}_\delta + \varepsilon\delta\boldsymbol{u}$, $\boldsymbol{e}_\partial = \boldsymbol{\varphi}_\partial + \varepsilon\partial\boldsymbol{u}$, and $\boldsymbol{e}_{\partial\delta} = \boldsymbol{\varphi}_{\partial\delta} + \varepsilon\partial\delta\boldsymbol{u}$ are introduced. It can be shown that the dual vector $\boldsymbol{e}$ and the helix $\boldsymbol{\eta}$ are related by $\boldsymbol{e} = \boldsymbol{\Gamma}^{\mathrm{T}}X'^{\mathrm{T}}\boldsymbol{\eta}$, and the relevant variation variables by

$$
\boldsymbol{e}_\delta = X'^{\mathrm{T}}\boldsymbol{\eta}_\delta, \quad \boldsymbol{e}_\partial = X'^{\mathrm{T}}\boldsymbol{\eta}_\partial, \quad \boldsymbol{e}_{\partial\delta} = X'^{\mathrm{T}}\boldsymbol{\eta}_{\partial\delta} + \tfrac{1}{2}(\boldsymbol{\varphi}_\partial\times X'^{\mathrm{T}}\boldsymbol{\eta}_\delta + \boldsymbol{\varphi}_\delta\times X'^{\mathrm{T}}\boldsymbol{\eta}_\partial),
$$

see [Merlini 2008a]. Thus, (7) are finally brought to the form

$$
\Pi_{bc\delta} = -\int_{L_c}\left\{\begin{matrix}\boldsymbol{\eta}_\delta\\ \delta\check{\boldsymbol{r}}_c\end{matrix}\right\}^{\mathrm{T}}\cdot\left\{\begin{matrix}\boldsymbol{R}_{c\eta}^{L}\\ \boldsymbol{R}_{cr}^{L}\end{matrix}\right\}\mathrm{d}L_c,
$$

$$
\partial\Pi_{bc\delta} = -\int_{L_c}\left(\left\{\begin{matrix}\boldsymbol{\eta}_\delta\\ \delta\check{\boldsymbol{r}}_c\end{matrix}\right\}^{\mathrm{T}}\cdot\left[\begin{matrix}\boldsymbol{D}_{c\eta\eta}^{L} & \boldsymbol{D}_{c\eta r}^{L}\\ \boldsymbol{D}_{c\eta r}^{L\,\mathrm{T}} & \mathbf{0}\end{matrix}\right]\cdot\left\{\begin{matrix}\boldsymbol{\eta}_\partial\\ \partial\check{\boldsymbol{r}}_c\end{matrix}\right\} + \left\{\begin{matrix}\boldsymbol{\eta}_{\partial\delta}\\ \partial\delta\check{\boldsymbol{r}}_c\end{matrix}\right\}^{\mathrm{T}}\cdot\left\{\begin{matrix}\boldsymbol{R}_{c\eta}^{L}\\ \boldsymbol{R}_{cr}^{L}\end{matrix}\right\}\right)\mathrm{d}L_c,
\tag{8}
$$

where

$$
\begin{aligned}
\{\boldsymbol{R}_{c\eta}^{L}\} &= \left\{\begin{matrix}\boldsymbol{Q}_{\mathrm{IIc}}\check{\boldsymbol{m}}_c + \boldsymbol{x}'\times N\check{\boldsymbol{t}}_c\\ N\check{\boldsymbol{t}}_c\end{matrix}\right\},\\
\{\boldsymbol{R}_{cr}^{L}\} &= \left\{\begin{matrix}\boldsymbol{Q}_{\mathrm{Ic}}\\ \boldsymbol{Q}_{\mathrm{Lc}}\end{matrix}\right\},\\
[\boldsymbol{D}_{c\eta\eta}^{L}] &= \left[\begin{matrix}\boldsymbol{\Gamma}^{-\mathrm{T}}(\check{\boldsymbol{m}}_c\cdot\boldsymbol{Q}_{\mathrm{IIIc}})\boldsymbol{\Gamma}^{-1} + \tfrac{1}{2}(\boldsymbol{Q}_{\mathrm{IIc}}\check{\boldsymbol{m}}_c)\times + \tfrac{1}{2}\big(\boldsymbol{x}'\times(N\check{\boldsymbol{t}}_c)\times + (N\check{\boldsymbol{t}}_c)\times\boldsymbol{x}'\times\big) & \tfrac{1}{2}(N\check{\boldsymbol{t}}_c)\times^{\mathrm{T}}\\ \tfrac{1}{2}(N\check{\boldsymbol{t}}_c)\times & \mathbf{0}\end{matrix}\right],\\
[\boldsymbol{D}_{c\eta r}^{L}] &= \left[\begin{matrix}\boldsymbol{Q}_{\mathrm{IIc}} & \boldsymbol{x}'\times N\\ \mathbf{0} & N\end{matrix}\right].
\end{aligned}
\tag{9}
$$

Note that the mixed virtual-incremental variation variables are retained in the tangent functionals $\partial \Pi_{\text{ext}\delta}$ and $\partial \Pi_{\text{bc}\delta}$, in consideration of a possible nonlinear dependence of the local variables on the ultimate problem unknowns.

3. Finite elements

3.1. *Linearized discrete variational principle.* The virtual functionals discussed above are assembled as a sum of contributions from the appropriate elements according to the finite element method. Three kinds of element contributions are considered.

First, the material surface *shell element* itself: the integrals $\Pi_{\text{int}\delta} = \int_S \pi_{\text{int}\delta}\,dS$ and $\partial \Pi_{\text{int}\delta} = \int_S \partial \pi_{\text{int}\delta}\,dS$, relevant to the internal work as discussed in Part I, and part of the integrals $\Pi_{\text{ext}\delta}$ and $\partial \Pi_{\text{ext}\delta}$ from (6), relevant to the external loads, pertain to this element. So, recalling Part I, Equation (67), the virtual functional and the virtual tangent functional of the shell element, which spans over the surface S^e, are written

$$\Pi_\delta^{S^e} = \int_{S^e} \left(\left\{ \begin{matrix} \delta(\boldsymbol{H}^{\mathrm{T}}\boldsymbol{\omega}_\alpha) \\ \delta\hat{\boldsymbol{\tau}} \end{matrix} \right\}^{\mathrm{T}} \cdot \left\{ \begin{matrix} \boldsymbol{H}^{\mathrm{T}}\bar{\boldsymbol{R}}_{\boldsymbol{\omega}}^\alpha \\ \bar{\boldsymbol{R}}_{\boldsymbol{\tau}} \end{matrix} \right\} - \{\boldsymbol{\eta}_\delta\}^{\mathrm{T}} \cdot \{\boldsymbol{R}_{\mathrm{f}\eta}^S\} \right) dS^e,$$

$$\partial \Pi_\delta^{S^e} = \int_{S^e} \left(\left\{ \begin{matrix} \delta(\boldsymbol{H}^{\mathrm{T}}\boldsymbol{\omega}_\alpha) \\ \delta\hat{\boldsymbol{\tau}} \end{matrix} \right\}^{\mathrm{T}} \cdot \left[\begin{matrix} \boldsymbol{H}^{\mathrm{T}}\bar{\boldsymbol{D}}_{\boldsymbol{\omega}\boldsymbol{\omega}}^{\alpha\beta}\boldsymbol{H} & \boldsymbol{H}^{\mathrm{T}}\bar{\boldsymbol{D}}_{\boldsymbol{\omega}\boldsymbol{\tau}}^\alpha \\ \bar{\boldsymbol{D}}_{\boldsymbol{\omega}\boldsymbol{\tau}}^{\beta\mathrm{T}}\boldsymbol{H} & \bar{\boldsymbol{D}}_{\boldsymbol{\tau}\boldsymbol{\tau}} \end{matrix} \right] \cdot \left\{ \begin{matrix} \partial(\boldsymbol{H}^{\mathrm{T}}\boldsymbol{\omega}_\beta) \\ \partial\hat{\boldsymbol{\tau}} \end{matrix} \right\} - \{\boldsymbol{\eta}_\delta\}^{\mathrm{T}} \cdot [\boldsymbol{D}_{\mathrm{f}\eta\eta}^S] \cdot \{\boldsymbol{\eta}_\partial\} \right. \tag{10}$$

$$\left. + \left\{ \begin{matrix} \partial\delta(\boldsymbol{H}^{\mathrm{T}}\boldsymbol{\omega}_\alpha) \\ \partial\delta\hat{\boldsymbol{\tau}} \end{matrix} \right\}^{\mathrm{T}} \cdot \left\{ \begin{matrix} \boldsymbol{H}^{\mathrm{T}}\bar{\boldsymbol{R}}_{\boldsymbol{\omega}}^\alpha \\ \bar{\boldsymbol{R}}_{\boldsymbol{\tau}} \end{matrix} \right\} - \{\boldsymbol{\eta}_{\partial\delta}\}^{\mathrm{T}} \cdot \{\boldsymbol{R}_{\mathrm{f}\eta}^S\} \right) dS^e,$$

where tensors $\bar{\boldsymbol{R}}$ and $\bar{\boldsymbol{D}}$ are given in Part I, Equation (66).

Second, the *border load element*, to which the other terms in (6) relevant to the external loads pertain. It lies on the line L_{f}^e, and the relevant functionals are written

$$\Pi_\delta^{L_{\mathrm{f}}^e} = -\int_{L_{\mathrm{f}}^e} \{\boldsymbol{\eta}_\delta\}^{\mathrm{T}} \cdot \{\boldsymbol{R}_{\mathrm{f}\eta}^L\}\,dL_{\mathrm{f}}^e, \qquad \partial \Pi_\delta^{L_{\mathrm{f}}^e} = -\int_{L_{\mathrm{f}}^e} (\{\boldsymbol{\eta}_\delta\}^{\mathrm{T}} \cdot [\boldsymbol{D}_{\mathrm{f}\eta\eta}^L] \cdot \{\boldsymbol{\eta}_\partial\} + \{\boldsymbol{\eta}_{\partial\delta}\}^{\mathrm{T}} \cdot \{\boldsymbol{R}_{\mathrm{f}\eta}^L\})\,dL_{\mathrm{f}}^e. \tag{11}$$

This element is a useful means to introduce external loads distributed along the shell boundary.

Third, an element to implement the boundary constraints as for (8). However, in the present version of the finite element code, this element is not integrated over a line L_{c}^e, but instead is attached to a single node N_{c}^e; hence, it is referred to as the *node constraint element*. The relevant functionals are written

$$\Pi_\delta^{N_{\mathrm{c}}^e} = -\left\{ \begin{matrix} \boldsymbol{\eta}_{\delta J} \\ \delta\check{\boldsymbol{r}}_{\mathrm{c}J} \end{matrix} \right\}^{\mathrm{T}} \cdot \left\{ \begin{matrix} \boldsymbol{R}_{\mathrm{c}\eta}^N \\ \boldsymbol{R}_{\mathrm{c}r}^N \end{matrix} \right\},$$

$$\partial \Pi_\delta^{N_{\mathrm{c}}^e} = -\left(\left\{ \begin{matrix} \boldsymbol{\eta}_{\delta J} \\ \delta\check{\boldsymbol{r}}_{\mathrm{c}J} \end{matrix} \right\}^{\mathrm{T}} \cdot \left[\begin{matrix} \boldsymbol{D}_{\mathrm{c}\eta\eta}^N & \boldsymbol{D}_{\mathrm{c}\eta r}^N \\ \boldsymbol{D}_{\mathrm{c}\eta r}^{N\mathrm{T}} & \boldsymbol{0} \end{matrix} \right] \cdot \left\{ \begin{matrix} \boldsymbol{\eta}_{\partial J} \\ \partial\check{\boldsymbol{r}}_{\mathrm{c}J} \end{matrix} \right\} + \{\boldsymbol{\eta}_{\partial\delta J}\}^{\mathrm{T}} \cdot \{\boldsymbol{R}_{\mathrm{c}\eta}^N\} \right), \tag{12}$$

where $\boldsymbol{\eta}_J$ and $\check{\boldsymbol{r}}_{\mathrm{c}J}$ refer to the helix and the dual reaction at the constrained node J, and the dual vectors $\boldsymbol{R}_{\mathrm{c}}^N$ and tensors $\boldsymbol{D}_{\mathrm{c}}^N$ are evaluated from (9) at that node. Note that the mixed virtual-incremental variation $\partial\delta\check{\boldsymbol{r}}_{\mathrm{c}}$ has been discarded while passing from (8) to (12); in fact $\check{\boldsymbol{r}}_{\mathrm{c}J}$ is now an ultimate free unknown of

the discrete problem. This is not the case for $\boldsymbol{\eta}_{\partial\delta}$. The node constraint element is not specific to the shell modeling and can be used in any finite element analysis.

The linearized variational principle is therefore cast in the form $\Pi_\delta + \partial\Pi_\delta = 0$, where the discrete virtual functional and virtual tangent functional of the whole problem are built with the contribution from all the elements:

$$\Pi_\delta = \sum_{S^e} \Pi_\delta^{S^e} + \sum_{L_f^e} \Pi_\delta^{L_f^e} + \sum_{N_c^e} \Pi_\delta^{N_c^e}, \quad \partial\Pi_\delta = \sum_{S^e} \partial\Pi_\delta^{S^e} + \sum_{L_f^e} \partial\Pi_\delta^{L_f^e} + \sum_{N_c^e} \partial\Pi_\delta^{N_c^e}.$$

Note that the external loads and possibly the reaction constraints will contribute to the tangent stiffness.

3.2. *Element kinematic field.* As discussed in Part I, Section 3, the formulation of the material surface kinematics is based on the integral field of the rototranslations. Rototranslations are orthogonal dual tensors, and as such they compose multiplicatively and do not commute. These distinctive properties of the kinematic field should be preserved in the approximate, substitute field on which a surface element is built. The *helicoidal interpolation* developed in [Merlini and Morandini 2004b] fulfills this requirement and is adopted here for both the shell and the border load elements.

Given N nodal frames in space, with orientoposition tensors A_J ($J = 1, 2, \ldots, N$), the interpolated orientoposition A is determined by the equation

$$\sum_{J=1}^{N} W_J \log(A A_J^{\mathrm{T}}) = \mathbf{0}, \tag{13}$$

where W_J are N given weights that measure the influence of each frame J on the sought one. Solution of (13) yields the *weighted average orientoposition* A, that is, an orientoposition with a null weighted average of the logarithms of the relative rototranslations $\tilde{\boldsymbol{H}}_J = A A_J^{\mathrm{T}}$ from the nodal frames, hence with a null weighted average of the relative helices $\tilde{\boldsymbol{\eta}}_J$ from A_J to A (see Figure 2). In the present application, as in the solid elements [Merlini and Morandini 2005], Lagrange polynomial interpolants on rectangular domains are assumed; so, the proposed corner-node elements (4-node shell element and 2-node border load element) are built with standard multilinear weight functions W_J. It is worth noting, in Figure 2, that the nodal orientations control the orientation as well as the position of the interpolated point.

Equation (13) is an implicit nonlinear equation. In general, it cannot give the interpolated orientoposition A in closed form, however it can be solved numerically by a refined Newton–Raphson procedure that proves very efficient. Then, the spatial derivatives of the weight functions W_J with respect to the local curvilinear coordinates ξ^α allow us to compute the curvature dual vectors in closed form as

$$\boldsymbol{k}_\alpha = -(\boldsymbol{\Lambda}_{\mathrm{II}}^-)^{-1} \sum_{J=1}^{N} W_{J,\alpha} \tilde{\boldsymbol{\eta}}_J, \tag{14}$$

where

$$\boldsymbol{\Lambda}_{\mathrm{II}}^- = \sum_{J=1}^{N} W_J \tilde{\boldsymbol{\Lambda}}_J^{-1}, \quad \tilde{\boldsymbol{\Lambda}}_J = \mathrm{dexp}(\tilde{\boldsymbol{\eta}}_J \times).$$

The helicoidal interpolation, (13) and (14), is first performed in the reference, undeformed configuration (this operation also allows an accurate setting of elements with possibly curved geometry). Then,
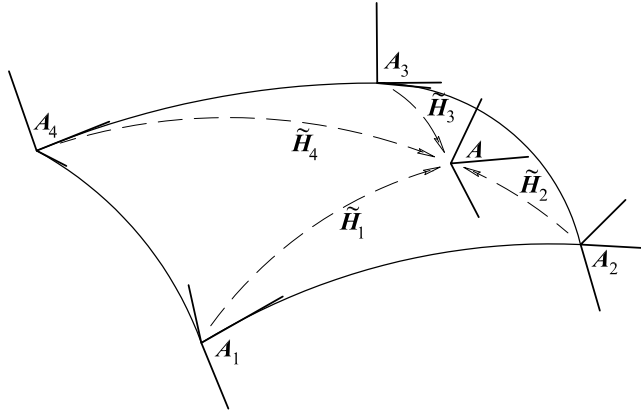
Figure 2. Helicoidal interpolation on a quadrilateral shell element.

the same interpolation scheme is applied to any current, deformed configuration; the comparison of the interpolated quantities between the current and the reference configurations allows us to recover (according to a total-Lagrangian approach) the local rototranslation $H = A'A^{\mathrm{T}}$ and the kinematical dual strains $\omega_\alpha = k'_\alpha - Hk_\alpha$ at the shell element quadrature points. It is worth stressing that this way of building the local kinematics is manifestly far from the customary standpoint of interpolating the rototranslations (or the rotations) of the nodal frames — a concept, in our opinion, devoid of consistency [Merlini and Morandini 2004b]. Note that operating on the orientopositions instead of the rototranslations makes this interpolation scheme path independent, as the local orientoposition and curvatures are computed independently from the past history of the nodal orientopositions. The proposed interpolation scheme is objective as well: the frame indifference and the invariance against rigid motions has been proved in [Merlini and Morandini 2004b], and is strictly connected to the concept of averaging the relative rototranslations from the nodal frames.

Evaluation of the integrals in (10) and (11) requires expressions for the virtual, incremental, and mixed virtual-incremental local variation variables. These are the outcome of the linearization of the helicoidal interpolation (13), a complicated process discussed in [Merlini and Morandini 2004b], that yields the local variation variables as linear functions of the relevant nodal variation variables. In the following, just the resulting interpolation formulae are written for the specific case of shell elements (see [Merlini and Morandini 2008]):

$$
\begin{aligned}
\{\boldsymbol{\eta}_\delta\} &= \sum_{J=1}^{N} [N_{\mathrm{A}J}] \cdot \{\boldsymbol{\eta}_{\delta J}\}, \\
\{\boldsymbol{\eta}_\partial\} &= \sum_{K=1}^{N} [N_{\mathrm{A}K}] \cdot \{\boldsymbol{\eta}_{\partial K}\}, \\
\{\boldsymbol{\eta}_{\partial\delta}\} &= \sum_{J=1}^{N} [N_{\mathrm{A}J}] \cdot \{\boldsymbol{\eta}_{\partial\delta J}\} + \sum_{J=1}^{N}\sum_{K=1}^{N} \left\{ \begin{array}{l} \{\boldsymbol{\eta}_{\delta J}\} \cdot [\mathcal{N}^{\mathrm{T}213}_{\mathrm{Aa}JK}] \cdot \{\boldsymbol{\eta}_{\partial K}\} \\ \{\boldsymbol{\eta}_{\delta J}\} \cdot [\mathcal{N}^{\mathrm{T}213}_{\mathrm{Al}JK}] \cdot \{\boldsymbol{\eta}_{\partial K}\} \end{array} \right\},
\end{aligned}
\tag{15}
$$

and

$$\{\boldsymbol{H}\delta(\boldsymbol{H}^{\mathrm{T}}\boldsymbol{\omega}_\alpha)\} = \sum_{J=1}^{N}[\mathcal{N}_{\mathrm{K}J\alpha}]\cdot\{\boldsymbol{\eta}_{\delta J}\},$$

$$\{\boldsymbol{H}\partial(\boldsymbol{H}^{\mathrm{T}}\boldsymbol{\omega}_\beta)\} = \sum_{K=1}^{N}[\mathcal{N}_{\mathrm{K}K\beta}]\cdot\{\boldsymbol{\eta}_{\partial K}\}, \tag{16}$$

$$\{\boldsymbol{H}\partial\delta(\boldsymbol{H}^{\mathrm{T}}\boldsymbol{\omega}_\alpha)\} = \sum_{J=1}^{N}[\mathcal{N}_{\mathrm{K}J\alpha}]\cdot\{\boldsymbol{\eta}_{\partial\delta J}\} + \sum_{J=1}^{N}\sum_{K=1}^{N}\left\{\begin{matrix}\{\boldsymbol{\eta}_{\delta J}\}\cdot[\mathbb{N}_{\mathrm{K}aJK\alpha}^{\mathrm{T}213}]\cdot\{\boldsymbol{\eta}_{\partial K}\}\\\{\boldsymbol{\eta}_{\delta J}\}\cdot[\mathbb{N}_{\mathrm{K}lJK\alpha}^{\mathrm{T}213}]\cdot\{\boldsymbol{\eta}_{\partial K}\}\end{matrix}\right\}.$$

It is worth noting that the linearization of the helicoidal interpolation supplies interpolation formulae capable of relating the mixed virtual-incremental local variation variables to the virtual, incremental, and mixed virtual-incremental nodal variation variables. The tensor matrices in (15) and (16) are defined as

$$[\boldsymbol{N}_{\mathrm{A}J}] = \begin{bmatrix}\mathrm{primal}\ \boldsymbol{V}_J & \boldsymbol{0}\\\mathrm{dual}\ \boldsymbol{V}_J & \mathrm{primal}\ \boldsymbol{V}_J\end{bmatrix},$$

$$[\mathcal{N}_{\mathrm{A}aJK}] = \begin{bmatrix}\mathrm{primal}\ \mathcal{V}_{JK} & \boldsymbol{0}\\\boldsymbol{0} & \boldsymbol{0}\end{bmatrix},$$

$$[\mathcal{N}_{\mathrm{A}lJK}] = \begin{bmatrix}\mathrm{dual}\ \mathcal{V}_{JK} & \mathrm{primal}\ \mathcal{V}_{JK}\\\mathrm{primal}\ \mathcal{V}_{JK} & \boldsymbol{0}\end{bmatrix},$$

and

$$[\mathcal{N}_{\mathrm{K}J\alpha}] = \begin{bmatrix}\mathrm{primal}\ \breve{\mathcal{W}}_{J\alpha} & \boldsymbol{0}\\\mathrm{dual}\ \breve{\mathcal{W}}_{J\alpha} & \mathrm{primal}\ \breve{\mathcal{W}}_{J\alpha}\end{bmatrix},$$

$$[\mathbb{N}_{\mathrm{K}aJK\alpha}] = \begin{bmatrix}\mathrm{primal}\ \breve{\mathbb{W}}_{JK\alpha} & \boldsymbol{0}\\\boldsymbol{0} & \boldsymbol{0}\end{bmatrix},$$

$$[\mathbb{N}_{\mathrm{K}lJK\alpha}] = \begin{bmatrix}\mathrm{dual}\ \breve{\mathbb{W}}_{JK\alpha} & \mathrm{primal}\ \breve{\mathbb{W}}_{JK\alpha}\\\mathrm{primal}\ \breve{\mathbb{W}}_{JK\alpha} & \boldsymbol{0}\end{bmatrix},$$

where

$$\breve{\mathcal{W}}_{J\alpha} = \mathcal{W}_{J\alpha} + \tfrac{1}{2}\boldsymbol{k}'_\alpha\times\boldsymbol{V}_J,$$

$$\breve{\mathbb{W}}_{JK\alpha} = \mathbb{W}_{JK\alpha} + \tfrac{1}{2}\boldsymbol{k}'_\alpha\times\mathcal{V}_{JK} + \tfrac{1}{2}(\boldsymbol{I}^{\times}\mathcal{W}_{J\alpha})^{\mathrm{T}132}\boldsymbol{V}_K + \tfrac{1}{2}((\boldsymbol{I}^{\times}\mathcal{W}_{K\alpha})^{\mathrm{T}132}\boldsymbol{V}_J)^{\mathrm{T}132} + ((\boldsymbol{I}\otimes\boldsymbol{k}'_\alpha)^{\mathrm{S}1\underline{23}}\boldsymbol{V}_J)^{\mathrm{T}132}\boldsymbol{V}_K,$$

and tensors $\boldsymbol{V}_J$, $\mathcal{V}_{JK}$, $\mathcal{W}_{J\alpha}$, and $\mathbb{W}_{JK\alpha}$ are defined in [Merlini and Morandini 2004b].

3.3. *Element Biot-axial field.* The so-called surface Biot-axial stress parameter $\hat{\boldsymbol{\tau}}$, which pertains to the Euclidean vector space, is approximated in a much simpler way: it is assumed *uniform* over the shell element domain, say

$$\hat{\boldsymbol{\tau}} = \hat{\boldsymbol{\tau}}_E,$$

with $\hat{\boldsymbol{\tau}}_E$ a discrete variable of the global problem, unique for the each single element. Linearization of $\hat{\boldsymbol{\tau}}$ is straightforward, $\delta\hat{\boldsymbol{\tau}} = \delta\hat{\boldsymbol{\tau}}_E$ and $\partial\hat{\boldsymbol{\tau}} = \partial\hat{\boldsymbol{\tau}}_E$, whereas of course $\partial\delta\hat{\boldsymbol{\tau}} = \boldsymbol{0}$, since $\hat{\boldsymbol{\tau}}_E$ is an ultimate free unknown of the discrete problem.

The choice of a uniform Biot-axial parameter is consistent with the interpolation of $\hat{\boldsymbol{\tau}}$ discussed in [Merlini and Morandini 2005] for the solid element, see the particular case of planar elements. Other interpolation schemes have been investigated [Merlini and Morandini 2008] and tested, however with less success.

3.4. *Element matrices.* Using the variation variables obtained in Sections 3.2 and 3.3 within (10)–(12), the element contributions to the virtual functional and virtual tangent functional are brought to the following form (details in [Merlini and Morandini 2008]).

- Shell element:

$$\Pi_\delta^{S^e} = \sum_{J=1}^4 \{\boldsymbol{\eta}_{\delta J}\}^{\mathrm{T}} \cdot \{\boldsymbol{F}_{\boldsymbol{\eta} J}^S\} + \delta\hat{\boldsymbol{\tau}}_E \cdot \boldsymbol{F}_{\boldsymbol{\tau} E}^S,$$

$$\partial\Pi_\delta^{S^e} = \sum_{J=1}^4 \sum_{K=1}^4 \{\boldsymbol{\eta}_{\delta J}\}^{\mathrm{T}} \cdot [\boldsymbol{K}_{\boldsymbol{\eta\eta} JK}^S] \cdot \{\boldsymbol{\eta}_{\partial K}\} + \sum_{J=1}^4 \{\boldsymbol{\eta}_{\delta J}\}^{\mathrm{T}} \cdot [\boldsymbol{K}_{\boldsymbol{\eta\tau} JE}^S] \cdot \partial\hat{\boldsymbol{\tau}}_E \tag{17}$$

$$+ \delta\hat{\boldsymbol{\tau}}_E \cdot \sum_{K=1}^4 [\boldsymbol{K}_{\boldsymbol{\eta\tau} KE}^S]^{\mathrm{T}} \cdot \{\boldsymbol{\eta}_{\partial K}\} + \delta\hat{\boldsymbol{\tau}}_E \cdot \boldsymbol{K}_{\boldsymbol{\tau\tau} EE}^S \cdot \partial\hat{\boldsymbol{\tau}}_E + \sum_{J=1}^4 \{\boldsymbol{\eta}_{\partial\delta J}\}^{\mathrm{T}} \cdot \{\boldsymbol{F}_{\boldsymbol{\eta} J}^S\}.$$

- Border load element:

$$\Pi_\delta^{L_{\mathrm{f}}^e} = \sum_{J=1}^2 \{\boldsymbol{\eta}_{\delta J}\}^{\mathrm{T}} \cdot \{\boldsymbol{F}_{\boldsymbol{\eta} J}^L\},$$

$$\partial\Pi_\delta^{L_{\mathrm{f}}^e} = \sum_{J=1}^2 \sum_{K=1}^2 \{\boldsymbol{\eta}_{\delta J}\}^{\mathrm{T}} \cdot [\boldsymbol{K}_{\boldsymbol{\eta\eta} JK}^L] \cdot \{\boldsymbol{\eta}_{\partial K}\} + \sum_{J=1}^2 \{\boldsymbol{\eta}_{\partial\delta J}\}^{\mathrm{T}} \cdot \{\boldsymbol{F}_{\boldsymbol{\eta} J}^L\}. \tag{18}$$

- Node constraint element:

$$\Pi_\delta^{N_{\mathrm{c}}^e} = \{\boldsymbol{\eta}_{\delta J}\}^{\mathrm{T}} \cdot \{\boldsymbol{F}_{\boldsymbol{\eta} J}^N\} + \{\delta\check{\boldsymbol{r}}_{\mathrm{c} J}\}^{\mathrm{T}} \cdot \{\boldsymbol{F}_{\boldsymbol{r} J}^N\},$$

$$\partial\Pi_\delta^{N_{\mathrm{c}}^e} = \{\boldsymbol{\eta}_{\delta J}\}^{\mathrm{T}} \cdot [\boldsymbol{K}_{\boldsymbol{\eta\eta} JJ}^N] \cdot \{\boldsymbol{\eta}_{\partial J}\} + \{\boldsymbol{\eta}_{\delta J}\}^{\mathrm{T}} \cdot [\boldsymbol{K}_{\boldsymbol{\eta r} JJ}^N] \cdot \{\partial\check{\boldsymbol{r}}_{\mathrm{c} J}\} \tag{19}$$

$$+ \{\delta\check{\boldsymbol{r}}_{\mathrm{c} J}\}^{\mathrm{T}} \cdot [\boldsymbol{K}_{\boldsymbol{\eta r} JJ}^N]^{\mathrm{T}} \cdot \{\boldsymbol{\eta}_{\partial J}\} + \{\boldsymbol{\eta}_{\partial\delta J}\}^{\mathrm{T}} \cdot \{\boldsymbol{F}_{\boldsymbol{\eta} J}^N\}.$$

Equations (17)–(19) can be directly assembled within the global variational functionals of the whole discrete problem. The element contributions to the problem residual and tangent matrix are as follows.

- Shell element:

$$\{\boldsymbol{F}_{\boldsymbol{\eta} J}^S\} = \int_{S^e} (\{\bar{\boldsymbol{R}}_{\boldsymbol{\omega}}^\alpha\}^{\mathrm{T}} \cdot [\mathscr{N}_{\mathrm{K} J\alpha}] - \{\boldsymbol{R}_{\mathrm{f}\boldsymbol{\eta}}^S\}^{\mathrm{T}} \cdot [N_{\mathrm{A} J}]) \, \mathrm{d}S^e,$$

$$\boldsymbol{F}_{\boldsymbol{\tau} E}^S = \int_{S^e} \bar{\boldsymbol{R}}_{\boldsymbol{\tau}} \, \mathrm{d}S^e,$$

$$[\boldsymbol{K}_{\boldsymbol{\eta\eta} JK}^S] = \int_{S^e} ([\mathscr{N}_{\mathrm{K} J\alpha}]^{\mathrm{T}} \cdot [\bar{\boldsymbol{D}}_{\boldsymbol{\omega\omega}}^{\alpha\beta}] \cdot [\mathscr{N}_{\mathrm{K} K\beta}] + [\text{dual } \bar{\boldsymbol{R}}_{\boldsymbol{\omega}}^\alpha \cdot \mathbb{N}_{\mathrm{Ka} JK\alpha}] + [\text{primal } \bar{\boldsymbol{R}}_{\boldsymbol{\omega}}^\alpha \cdot \mathbb{N}_{\mathrm{Kl} JK\alpha}]$$

$$- [N_{\mathrm{A} J}]^{\mathrm{T}} \cdot [\boldsymbol{D}_{\mathrm{f}\boldsymbol{\eta\eta}}^S] \cdot [N_{\mathrm{A} K}] - [\text{dual } \boldsymbol{R}_{\mathrm{f}\boldsymbol{\eta}}^S \cdot \mathscr{N}_{\mathrm{Aa} JK}] - [\text{primal } \boldsymbol{R}_{\mathrm{f}\boldsymbol{\eta}}^S \cdot \mathscr{N}_{\mathrm{Al} JK}]) \, \mathrm{d}S^e,$$

$$[\boldsymbol{K}_{\eta\tau JE}^{S}] = \int_{S^e} [\mathcal{N}_{KJ\alpha}]^{\mathrm{T}} \cdot [\overline{\boldsymbol{D}}_{\omega\tau}^{\alpha}] \mathrm{d}S^e,$$

$$\boldsymbol{K}_{\tau\tau EE}^{S} = \int_{S^e} \overline{\boldsymbol{D}}_{\tau\tau} \,\mathrm{d}S^e.$$

- Border load element:

$$\{\boldsymbol{F}_{\eta J}^{L}\} = \int_{L_{\mathrm{f}}^e} (-\{\boldsymbol{R}_{\mathrm{f}\eta}^{L}\}^{\mathrm{T}} \cdot [N_{\mathrm{A}J}]) \,\mathrm{d}L_{\mathrm{f}}^e,$$

$$[\boldsymbol{K}_{\eta\eta JK}^{L}] = \int_{L_{\mathrm{f}}^e} (-[N_{\mathrm{A}J}]^{\mathrm{T}} \cdot [\boldsymbol{D}_{\mathrm{f}\eta\eta}^{L}] \cdot [N_{\mathrm{A}K}] - [\text{dual } \boldsymbol{R}_{\mathrm{f}\eta}^{L} \cdot \mathcal{N}_{\mathrm{Aa}JK}] - [\text{primal } \boldsymbol{R}_{\mathrm{f}\eta}^{L} \cdot \mathcal{N}_{\mathrm{Al}JK}]) \,\mathrm{d}L_{\mathrm{f}}^e.$$

- Node constraint element:

$$\{\boldsymbol{F}_{\eta J}^{N}\} = -\{\boldsymbol{R}_{\mathrm{c}\eta}^{N}\}, \quad \{\boldsymbol{F}_{rJ}^{N}\} = -\{\boldsymbol{R}_{\mathrm{c}r}^{N}\}, \quad [\boldsymbol{K}_{\eta\eta JJ}^{N}] = -[\boldsymbol{D}_{\mathrm{c}\eta\eta}^{N}], \quad [\boldsymbol{K}_{\eta rJJ}^{N}] = -[\boldsymbol{D}_{\mathrm{c}\eta r}^{N}].$$

3.5. *Nodal mixed variation variables.* It is noted that $(17)_2$, $(18)_2$, and $(19)_2$ contain terms in the mixed virtual-incremental variation variables $\boldsymbol{\eta}_{\partial\delta J}$ relevant to the nodal helices. Before assembling the problem matrix, these mixed variation variables must be solved for the simple variation variables $\boldsymbol{\eta}_{\delta J}$ and $\boldsymbol{\eta}_{\partial J}$. The resolution of $\boldsymbol{\eta}_{\partial\delta J}$ is now possible at the nodes, since there the nodal helices are actually free variables. As explained in [Merlini and Morandini 2004b; 2005], using the differential map of the rototranslation and discarding, of course, the term $\partial\delta\boldsymbol{\eta}_J$, the resolution formula is easily obtained:

$$\boldsymbol{\eta}_{\partial\delta J} = \boldsymbol{\Lambda}_J \boldsymbol{\Lambda}_{\mathrm{III}J}^{-123} : \boldsymbol{\eta}_{\delta J} \otimes \boldsymbol{\eta}_{\partial J}. \tag{20}$$

Here, $\boldsymbol{\Lambda}_J$ and $\boldsymbol{\Lambda}_{\mathrm{III}J}^{-123}$ are the first and second differential mapping tensors associated with the exponential map of the nodal rototranslation $\boldsymbol{H}_J$; they are built with the current value of the nodal helix $\boldsymbol{\eta}_J$.

Using (20), terms of the type $\{\boldsymbol{\eta}_{\partial\delta J}\}^{\mathrm{T}} \cdot \{\boldsymbol{F}_J\}$ in (17)–(19) are transformed to $\{\boldsymbol{\eta}_{\delta J}\}^{\mathrm{T}} \cdot [\boldsymbol{K}_{JJ}] \cdot \{\boldsymbol{\eta}_{\partial J}\}$, where

$$[\boldsymbol{K}_{JJ}]$$
$$= \begin{bmatrix} \text{dual } \boldsymbol{F}_J \cdot \text{primal}(\boldsymbol{\Lambda}_J \boldsymbol{\Lambda}_{\mathrm{III}J}^{-123}) + \text{primal } \boldsymbol{F}_J \cdot \text{dual}(\boldsymbol{\Lambda}_J \boldsymbol{\Lambda}_{\mathrm{III}J}^{-123}) & \text{primal } \boldsymbol{F}_J \cdot \text{primal}(\boldsymbol{\Lambda}_J \boldsymbol{\Lambda}_{\mathrm{III}J}^{-123}) \\ \text{primal } \boldsymbol{F}_J \cdot \text{primal}(\boldsymbol{\Lambda}_J \boldsymbol{\Lambda}_{\mathrm{III}J}^{-123}) & \boldsymbol{0} \end{bmatrix}. \tag{21}$$

4. Numerical tests

The elements so far described have been implemented in the authors' own finite-element code, already used in the past computations with solid elements. The code, written in C++ language, is object-oriented and is equipped with an original geometrical library to help in manipulating high-order tensors. The surface elements exploit the Gauss quadrature rule with three integration points per local coordinate. At each surface quadrature point, the shell model is integrated across the thickness by the Gauss rule with two integration points along ξ^3 over the domain $[-1, +1]$. This choice of the through-the-thickness domain implies that in the present element version, the material surface lies on the mid shell surface. The characteristic length h is chosen as half the shell thickness, so the third base vector $\boldsymbol{g}_3$ (Part I, Equation (13)) is the normal segment from the mid surface to the outer surface at $\xi^3 = +1$ in the reference

configuration. The reference director is chosen as a pure dual vector $\boldsymbol{\theta} = \varepsilon h \boldsymbol{\alpha}^{\mathrm{T}} \boldsymbol{n}$, so that $\boldsymbol{k}_3 = \varepsilon h \boldsymbol{n}$ and $\boldsymbol{g}^{*3} = \boldsymbol{g}^3 = h\boldsymbol{n}$ is constant across the thickness. The target loads on the shell element and on the border load element are assigned by the user as density properties pertaining to each surface quadrature point.

Most test cases concern linear elastic isotropic materials. Since in the present variational formulation the strain-energy density w^* is by assumption a function of the Biot strain $\boldsymbol{\varepsilon}^{*\mathrm{S}}$ instead of the classical Green strain (see Part I, Section 5.1), the linear constitutive law analogous to the Saint Venant–Kirchhoff law descends from the hyperelastic strain-energy function

$$w^*(\boldsymbol{\varepsilon}^{*\mathrm{S}}) = \tfrac{1}{2} \hat{\lambda} (\operatorname{tr} \boldsymbol{\varepsilon}^{*\mathrm{S}})^2 + \hat{\mu} \operatorname{tr}(\boldsymbol{\varepsilon}^{*\mathrm{S}})^2,$$

where $\hat{\lambda}$ and $\hat{\mu}$ are Lamé moduli proper of the Biot-type parameterization. Using such a linear constitutive law instead of adapting the original Saint Venant–Kirchhoff law induces an error that is negligible as long as the strains remain small. This is the case of all the linear-material examples presented below; in the examples, the material data are given as an elastic modulus E and a Poisson ratio ν, from which the Lamé moduli are computed as usual as $\hat{\lambda} = E\nu/(1+\nu)(1-2\nu)$ and $\hat{\mu} = E/2(1+\nu)$. Besides the linear constitutive law, a classical neo-Hookean constitutive law is available; it descends, for the Biot-type parameterization, from the strain-energy function [Merlini and Morandini 2005]

$$w^*(\boldsymbol{U}^*) = \tfrac{1}{2} \lambda (\ln \det \boldsymbol{U}^*)^2 - \mu \ln \det \boldsymbol{U}^* + \tfrac{1}{2} \mu \operatorname{tr}(\boldsymbol{U}^{*2} - \boldsymbol{I}), \tag{22}$$

with $\boldsymbol{U}^* = \boldsymbol{I} + \boldsymbol{\varepsilon}^{*\mathrm{S}}$ the Cosserat deformation tensor.

The standard nonlinear solution is achieved by subsequent load steps. At each step, an iterative procedure of the Newton–Raphson kind is started. At each iteration, the nodal orientopositions are updated multiplicatively, $\boldsymbol{A}'_J \leftarrow \exp(\boldsymbol{\eta}_{\partial J} \times) \boldsymbol{A}'_J$, whereas the Biot-axial and reaction unknowns are updated additively. At the time of solving the linearized equations, the kinematical unknowns are transformed to become self-based, as described in [Merlini and Morandini 2005]. The solution of snapping and buckling problems is achieved by an arc-length procedure based on a modified Riks algorithm of the spherical type; implementation details and relevant references are given in [Merlini and Morandini 2008]. Both the monotone procedure and the arc-length procedure are equipped with an automatic step control, which makes the load-step size (respectively, the arc-step size) shrink or stretch dynamically.

Different convergence criteria are applied to the different subsets of the residual, work-conjugate respectively to the angular and linear parts of the kinematical variables, the constraint reactions, and the Biot-axial parameters. For each subset relevant to a single kind of kinematical variable, the maximum absolute value is first normalized with respect to the average of all the absolute contributions to that subset in the assembling process, then is requested to lower below 5×10^{-3}. For the other subsets, the maximum absolute value must vanish with a tolerance of 10^{-5}. Finally, the Euclidean norm of the whole computed solution must be less that 10^{-3}.

In the following examples, the helicoidal shell element is referred to as the HSE. It is worth emphasizing that in the pictures of the finite element models, the element geometry is built from the corner orientopositions by the helicoidal interpolation itself. This means that in the problem analysis, the quadrature points are located exactly where they can be actually imagined to stay, in local curvilinear coordinates, on the images (for example, observe Figure 3). No units are explicitly used in the examples, so it is understood that all measures in each test are associated with a coherent system of units, for example, SI.

Internal radius = 6
External radius = 10
Thickness = 0.03
Elastic modulus $E = 21 \times 10^6$
Poisson ratio $\nu = 0$
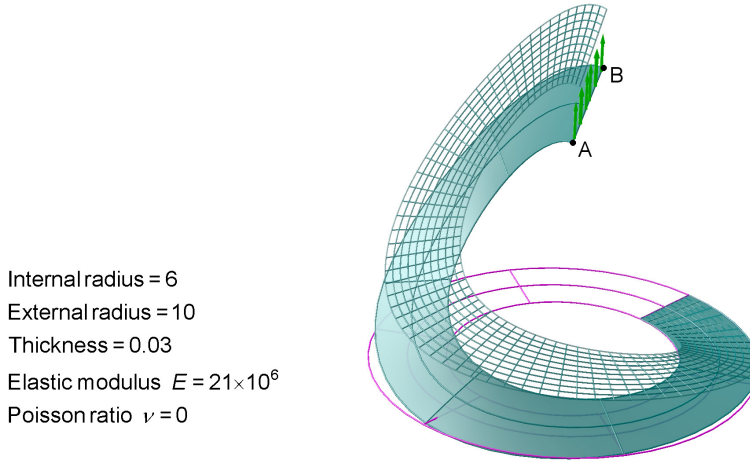
Figure 3. Slit annular plate: meshes of 2×6 and 10×70 at the final load (force/length $= 1$).

4.1. *Slit annular plate.* The slit annular plate was introduced in [Başar et al. 1992] as a benchmark problem for finite rotation formulations in geometrically nonlinear shell problems. Since then, most investigators have used this example to test the performance of shell elements, in [Wriggers and Gruttmann 1993; Ibrahimbegović and Frey 1994; Sansour and Kollmann 2000; Sze et al. 2002; Fontes Valente et al. 2003; Campello et al. 2003; Cardoso and Yoon 2005; Areias et al. 2005; Arciniega and Reddy 2007], among others. One edge of a slit ring plate is clamped, while the other edge is subjected to a transverse line load, which induces strong distortions in the originally plane elements. The problem data and the notable deformation of a coarse mesh of twelve HSE curved elements are shown in Figure 3. The distributed force is applied by a string of border load elements.

The free edge displacements with increasing load are plotted in Figure 4 for three different meshes and compared with the best results reported by [Sze et al. 2004]. The results from [Li and Zhan 2000], obtained with a shell element endowed with the drilling degree of freedom and based on Biot strain, are included in Figure 4. The convergence of the HSE and a very good agreement with the computations found in the literature are observed. Displacements every 0.2 force/length are reported in Table 1. Using such refined meshes, a high number of steps (130–140, with an average of 5–6 iterations per step) is necessary to reach the final solution (force/length $= 1$) by the monotone loading procedure.

	w_A			w_B		
Force/length	6×30	8×48	10×70	6×30	8×48	10×70
0.2	7.576	7.584	7.586	10.258	10.267	10.270
0.4	10.391	10.422	10.433	13.691	13.722	13.733
0.6	12.147	12.224	12.250	15.680	15.756	15.782
0.8	13.653	13.772	13.811	17.290	17.410	17.449
1.0	14.972	15.128	15.175	18.663	18.820	18.867

**Table 1.** Slit annular plate: displacements of points A and B with three different meshes.
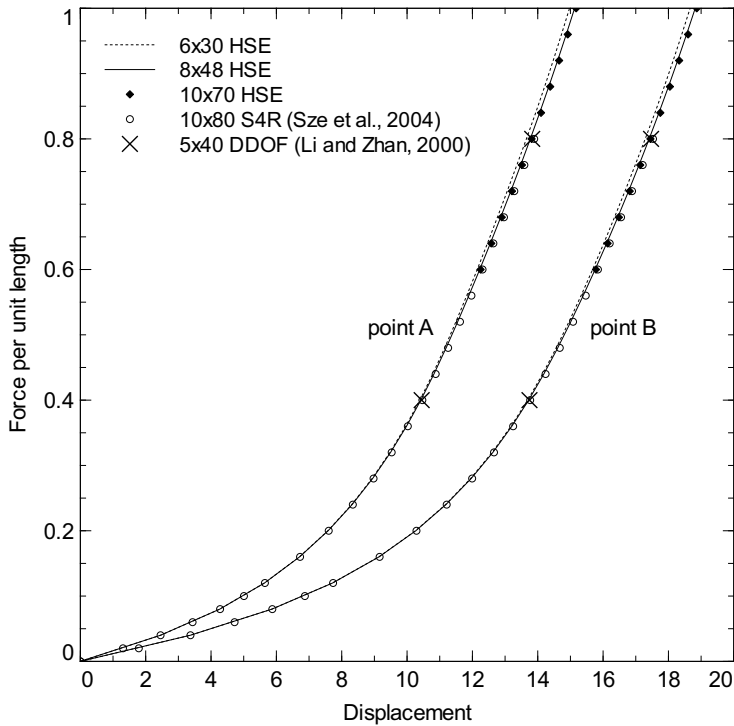
Figure 4. Slit annular plate: load-displacement curves.

4.2. *Twisted beam.* The example of a straight twisted strip, clamped at one end and loaded at the other end by a transverse force, was studied in the nonlinear regime by [Sansour and Kollmann 2000; Chróś-cielewski and Witkowski 2006]. The problem data are given in Figure 5. The analysis is performed on two meshes: 2×24 and 4×48 warped HSEs. The load is assigned as a distributed force along the tip edge in its own plane, by means of border load elements. The total load versus the tip deflections is plotted
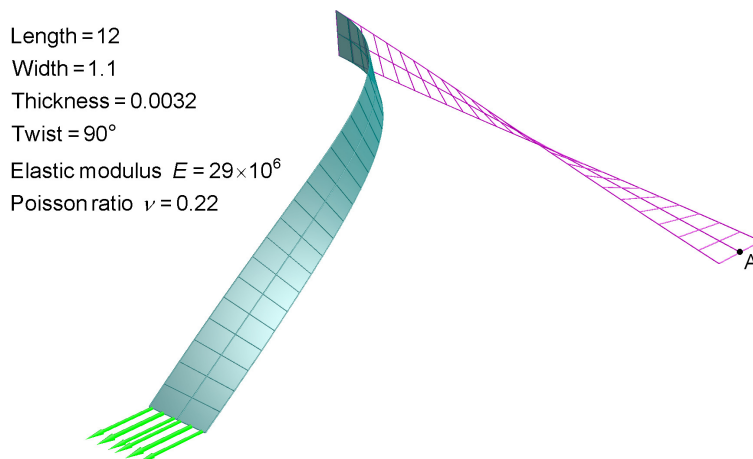
Figure 5. Twisted beam: 2×24 mesh in the reference configuration and at load of 0.007.
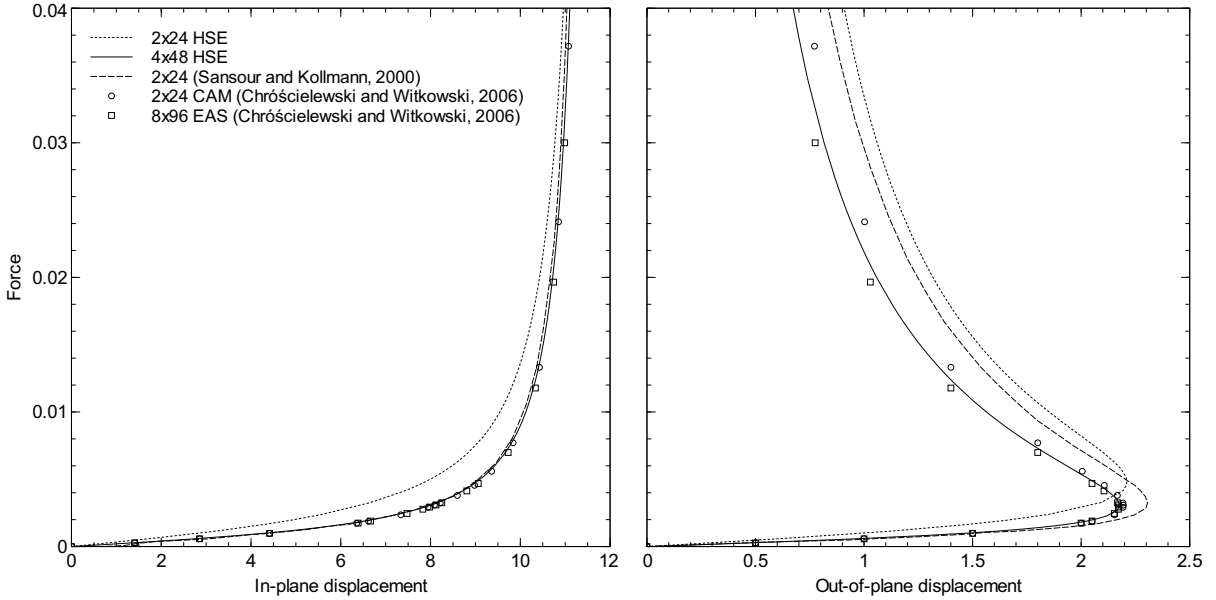
Figure 6. Twisted beam: displacements of tip A.

in Figure 6 and compared with results in the literature. This problem is a good benchmark to test the performance of elements with nonplanar geometry, and the behavior of the HSE seems satisfactory. Some representative displacements are listed in Table 2. The computation is very demanding in this case: with the 2×24 mesh the final load of 0.04 is reached in 194 load steps with an average of 6 iterations per step.

This example is also used to report the computed values of the Biot-axial variables in a shell analysis. The symmetric and skew-symmetric parts of the Biot stress within the three-dimensional domain across

2×24			4×48		
Force $\times 10^2$	In-plane	Out-of-plane	Force $\times 10^2$	In-plane	Out-of-plane
0.059	1.754	0.620	0.056	2.675	0.939
0.163	4.264	1.466	0.163	6.010	1.924
0.238	5.568	1.846	0.228	7.121	2.119
0.327	6.665	2.092	0.324	8.131	2.173
0.416	7.447	2.194	0.414	8.717	2.121
0.457	7.730	2.208	0.456	8.922	2.083
0.578	8.386	2.182	0.597	9.421	1.937
0.814	9.169	2.006	0.821	9.888	1.714
0.987	9.523	1.863	1.000	10.123	1.564
2.003	10.430	1.316	2.000	10.721	1.058
2.967	10.761	1.067	3.000	10.963	0.816
4.000	10.960	0.909	4.000	11.102	0.674

Table 2. Twisted beam: displacements of tip A up to load of 0.04 with two different meshes.
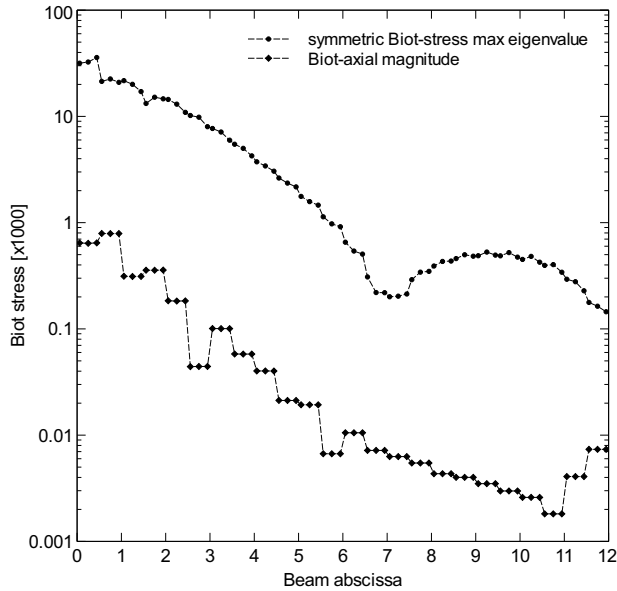
Figure 7. Twisted beam: $\max(\text{abs}(\text{eigenvalue}(\hat{\boldsymbol{T}}^{*S})))$ and $\|\hat{\boldsymbol{\tau}}^{*}\|$ as representative values of the elastically defined and the workless parts of the Biot stress within the thickness with a 2×24 mesh at the final load of 0.04; plot of the highest values among the twelve Gauss points at each beam abscissa.

the thickness can be compared on a logarithmic scale in Figure 7. The Biot-axial keeps lower than the elastically defined stress by at least one order of magnitude, and features an alternate course as already noticed in full three-dimensional analyses [Merlini and Morandini 2005]. Note that the perfect symmetry of the Biot stress within an isotropic material (see [Bufler 1985]) is lost in the present approximate analysis where the field equations are satisfied in a weak sense — a fact that confirms the computational role of the Biot-axial in a discrete model. The material surface Biot-axial parameter $\hat{\boldsymbol{\tau}}$ is modeled as a vector field uniform over the shell element. In the present computation, it is almost normal to the element surface and is distributed along the strip as the bar graph of Figure 8. The highest values of the Biot-axial are observed near the clamped side.
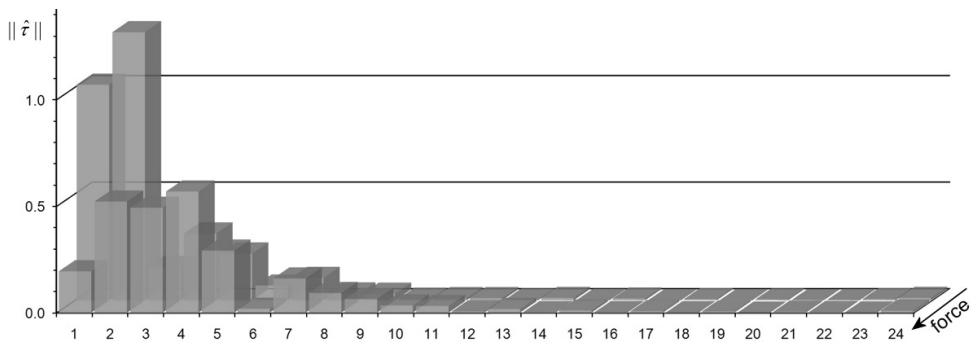
Figure 8. Twisted beam: magnitude of the surface Biot-axial parameter on the elements of a 2×24 mesh at the final load of 0.04.

Overall length = 30
Radius = 9
Thickness $t = 0.2$ or 2.0
Elastic parameters:
  $\lambda = 24000$, $\mu = 6000$
  ($E = 16800$, $\nu = 0.4$)
or:
  $\lambda = 240000$, $\mu = 6000$
  ($E = 17854$, $\nu = 0.4878$)
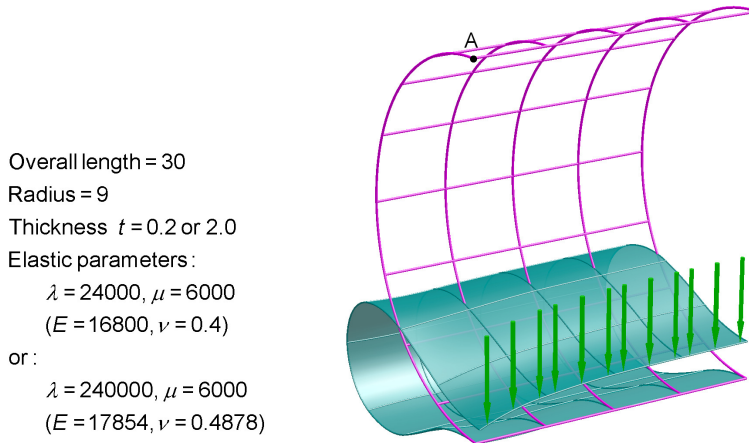
Figure 9. Cylindrical shell under line load: 8×4 mesh of a quarter cylinder and deformed model of case $t = 2.0$ and $\nu = 0.4$ at load of 36000 (displacement of vertex A = 17.388).

4.3. *Cylindrical shell under line load.* The cylindrical shell pinched by a line load along a generatrix and simply supported at the opposite generatrix was studied in [Büchter et al. 1994] as a test case for shell elements with nonlinear hyperelastic material. The same compressible neo-Hookean constitutive law, derived from the strain-energy function (22), is used here. The cylinder geometry and properties are given in Figure 9: a thin shell ($t = 0.2$) and a thick shell ($t = 2.0$), with both a compressible ($\nu = 0.4$) and a nearly incompressible ($\nu = 0.4878$) material, are considered. Due to symmetry, one quarter of the cylinder is modeled; three different meshes of increasing refinement along the circumference are analyzed, 8×4, 12×4, and 16×4 curved HSEs; the line load is introduced by four border load elements. A deformed model is also shown in Figure 9.

Portions of the load-displacement plots are shown in Figure 10. For the compressible material (Figures 10a and 10c), a comparison can be made with several shell elements based on 5, 6, and 7-parameter models and exploiting incompatible modes and EAS concepts, as proposed in [Büchter et al. 1994; Brank et al. 2002; Brank 2005] (in the last two of these papers, a slightly different constitutive law is used). The formulation of the HSE does not involve incompatible modes nor assumed strains, and the behavior of the HSE is apparently stiffer than the elements in the literature, in particular for the thick shell. It can be noted that the adaptation of the local constitutive law for the helicoidal shell model, as discussed in Part I, enables us to analyze nearly incompressible thin shells without resorting to any numerical expedient such as reduced integration. The effectiveness of this feature, however, seems to weaken as the shell thickness increases. For the nearly incompressible material (Figures 10b and 10d), no tests with shell elements have been found in the literature and a comparison could only be made with solid elements; published results with solid elements are not included in Figure 10 but can be found in [Reese et al. 2000; Merlini and Morandini 2005] and, with a different constitutive law, in [Chavan et al. 2007]. The computational burden of this test case is much less demanding: 25–35 load steps with about 6 iterations per step for the thin models and 8–12 steps with 9–10 iterations per step for the thick models.
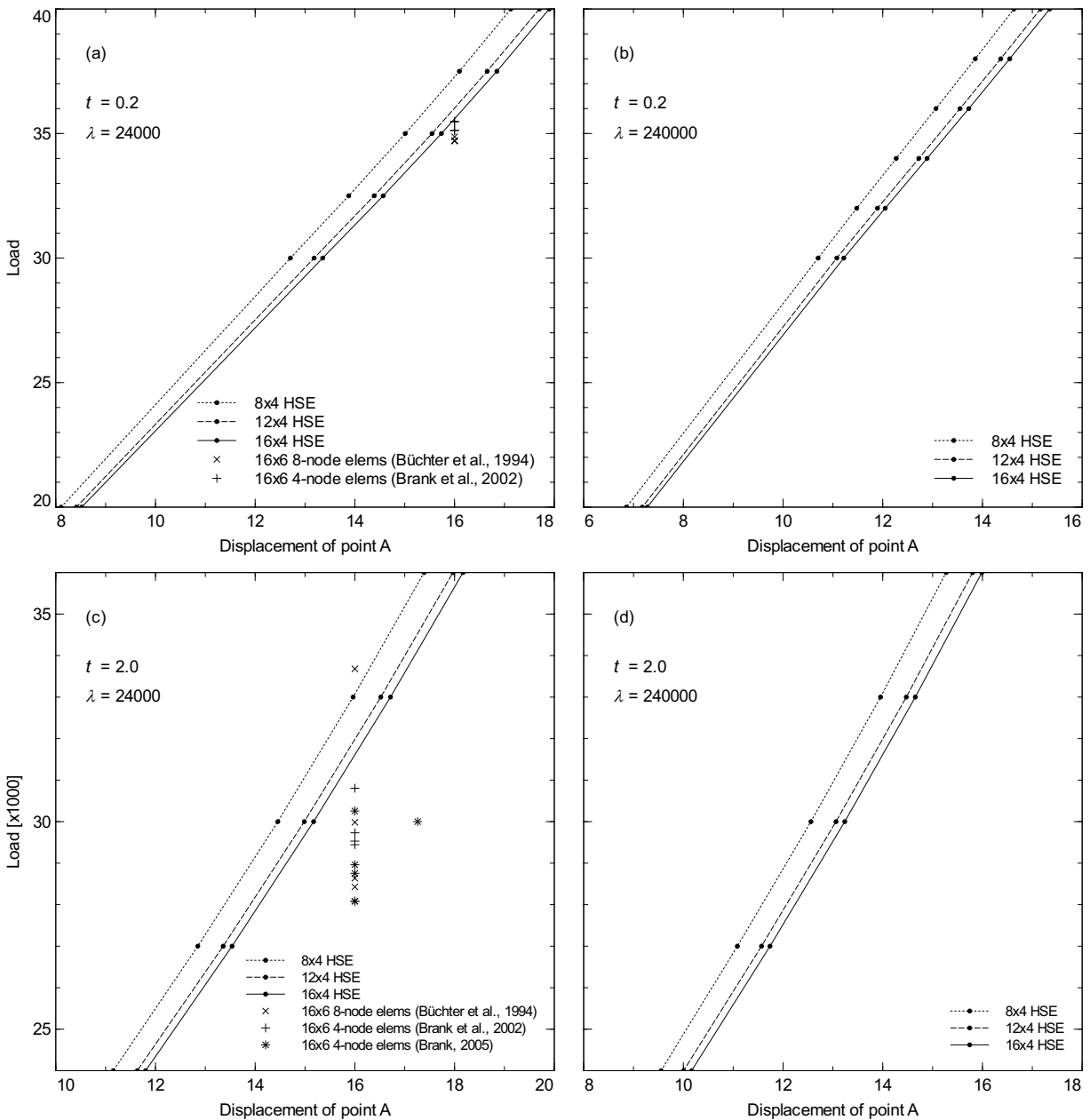
Figure 10. Cylindrical shell under line load: total load versus displacement of point A and some sparse values from literature.
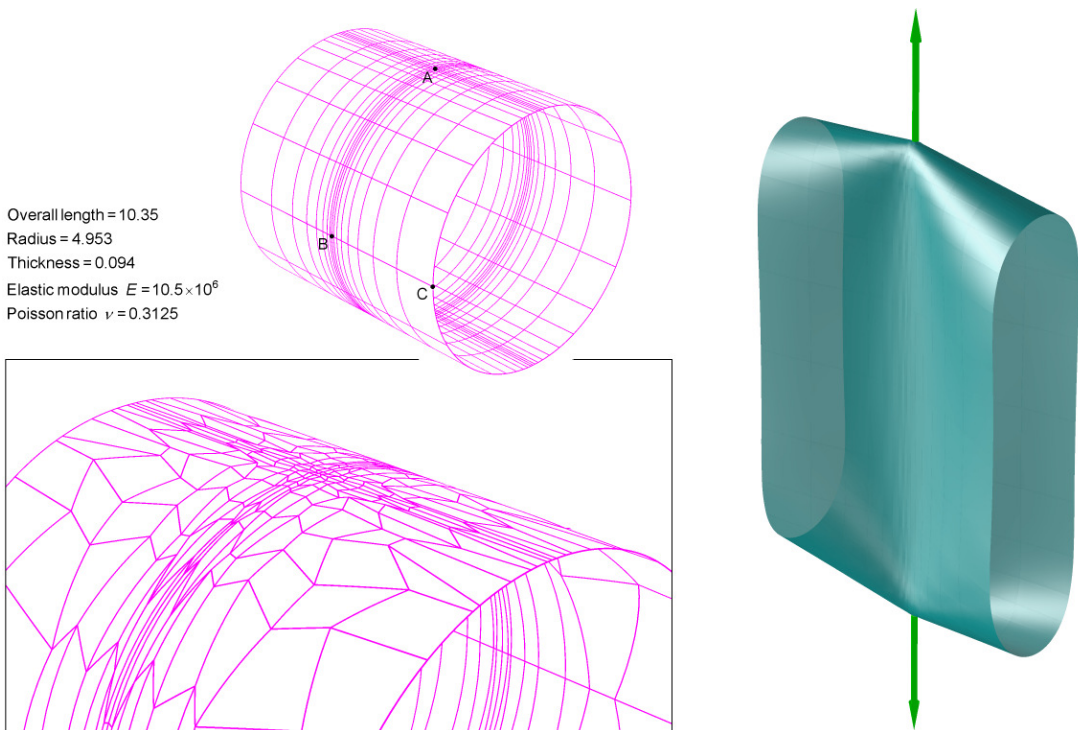
4.4. *Cylindrical shell pullout.* The cylinder stretched by two opposite forces is a very popular benchmark test in the shell element literature, for example, in [Sansour and Bufler 1992; Sansour and Bednarczyk 1995; Sansour and Kollmann 2000; Sze et al. 2002; Campello et al. 2003; Fontes Valente et al. 2003; Pimenta et al. 2004; Areias et al. 2005; Brank 2008], among others. The specimen is a cylindrical surface with open ends, pinched by two pulling forces along the mid diameter, see Figure 11. Due to

Node	1	2	3	4	5	6	7	8	9
y	0.00000	0.10506	0.26265	0.49903	0.85361	1.38547	2.18327	3.37996	5.17500

Table 3. Cylindrical shell pullout: node coordinates along the cylinder axis from point A (regular mesh).

symmetry, one octant of the cylinder is modeled using a mesh of 9×8 curved HSEs, with either a regular (rectangular) or an irregular pattern. The regular mesh has 9 elements in the circumferential direction and 8 elements in the axial direction. The coordinates of the first nine nodes from the load-point A in both directions are set by a geometric progression of common ratio 1.5 (see Table 3); the aspect ratio of the narrowest element is higher than 24. The irregular mesh is derived from the regular one by moving randomly the nodes in both directions within the range of half an element size: the quadrilaterals become very irregular, as evidenced in Figure 11.

Using the arc-length procedure, the target load of 40000 is exceeded in 23 steps with the regular mesh (6 iterations per step on average), and in 20 steps with the irregular one. In agreement with published results, a slight snap-through is observed at a load of about 20500. Plots of representative radial displacements at increasing load are shown in Figure 12: the reasonably similar results obtained with the two meshes are a clear evidence of the low sensitivity to irregular geometries of the proposed shell element. In Figure 12, the results from the present coarse regular mesh are successfully compared

Overall length = 10.35
Radius = 4.953
Thickness = 0.094
Elastic modulus $E = 10.5 \times 10^6$
Poisson ratio $\nu = 0.3125$

Figure 11. Cylindrical shell pullout: regular mesh in the reference configuration and at the final load of 40000; detail of the undeformed irregular mesh.
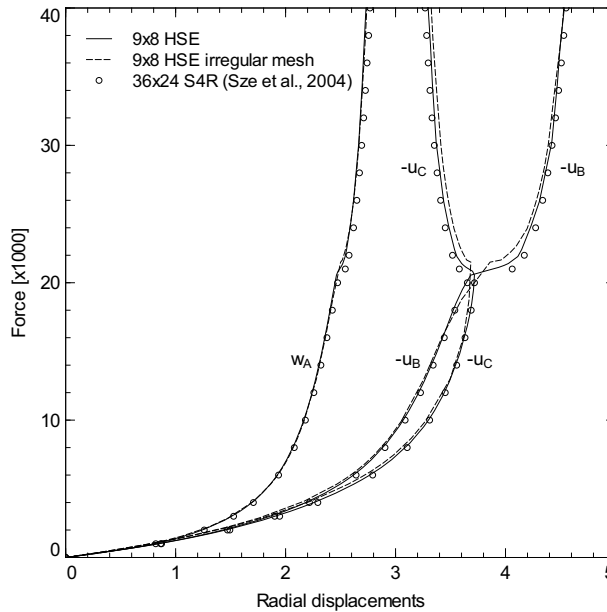
Figure 12. Cylindrical shell pullout: load-displacement curves.

with those obtained with a refined mesh in [Sze et al. 2004]. Loads and displacements at every history step are listed in Table 4.

4.5. *Pinched cylindrical shell with end diaphragms.* The cylinder pinched by two opposite point loads is another popular benchmark test; see for example, [Sansour and Bednarczyk 1995; Sansour and Kollmann 2000; Sze et al. 2002; Campello et al. 2003; Pimenta et al. 2004; Brank 2008]. The cylindrical shell is mounted over rigid end diaphragms that lock the in-plane displacements. Thus, the shell folds

Force	w_A	$-u_B$	$-u_C$	Force	w_A	$-u_B$	$-u_C$
625	0.561	0.551	0.556	10696	2.194	3.122	3.355
781	0.669	0.673	0.680	12806	2.268	3.260	3.490
952	0.776	0.800	0.808	16822	2.376	3.468	3.651
1140	0.881	0.931	0.941	18478	2.414	3.548	3.692
1460	1.036	1.136	1.150	20547	2.462	3.683	3.717
2055	1.262	1.461	1.485	21117	2.502	3.938	3.642
3345	1.583	1.985	2.039	21400	2.520	4.026	3.601
4018	1.696	2.189	2.263	22416	2.555	4.147	3.536
5341	1.861	2.498	2.621	25919	2.617	4.308	3.438
5974	1.921	2.612	2.759	34489	2.697	4.472	3.335
7129	2.011	2.782	2.966	42141	2.743	4.556	3.284
9524	2.144	3.031	3.257	40000	2.731	4.535	3.297

Table 4. Cylindrical shell pullout: radial displacements of points A, B, and C (regular mesh).

Overall length = 200
Radius = 100
Thickness = 1
Elastic modulus $E = 30 \times 10^3$
Poisson ratio $\nu = 0.3$
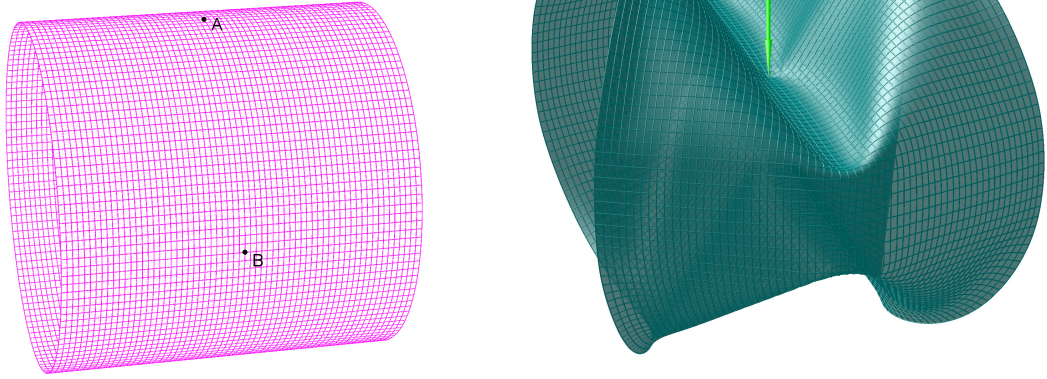
Figure 13. Pinched cylindrical shell with end diaphragms: deformed configuration at the final load of 12000.

notably under the two pushing forces directed as the mid diameter; see Figure 13. A refined, uniform mesh is appropriate to solve this problem: exploiting the problem symmetries, one octant of the cylinder is modeled by 32×32 curved HSEs. The analysis up to the final load of 12000 is performed by the arc-length procedure in 74 steps, with an average of 7 iterations per step. The load history exhibits several slight snap-throughs, as evidenced by the load-displacement plots of Figure 14. However, a
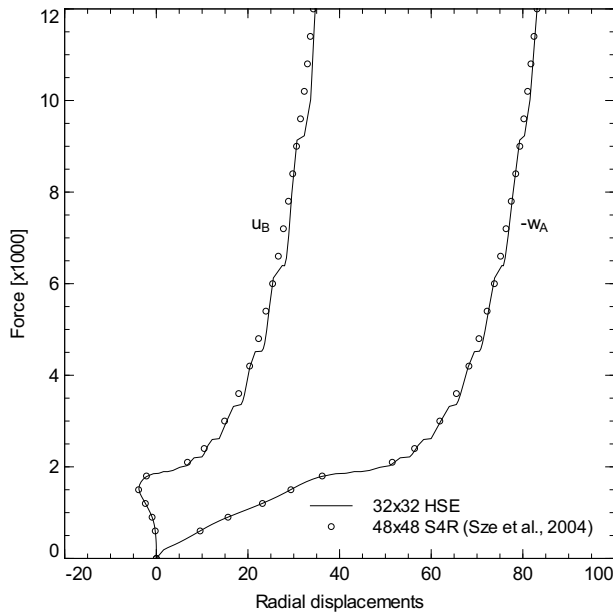
Figure 14. Pinched cylindrical shell with end diaphragms: load-displacement curves.

Force	$-w_A$	u_B
1003	18.171	-1.349
2026	50.980	6.683
4174	68.041	20.399
6125	73.842	25.550
7963	77.841	29.570
10017	81.570	33.686
12000	83.102	34.673

Table 5. Pinched cylindrical shell with end diaphragms: radial displacements of points A and B.

good agreement with the best results reported in [Sze et al. 2004] is observed. Some representative load-displacement pairs are listed in Table 5.

4.6. *Cylindrical roof under point load.* The buckling problem of the shallow cylindrical panel hinged along two generatrices and subjected to a central point load has been considered by several authors; refer to [Simo et al. 1990; Chróścielewski et al. 1992; Gruttmann et al. 1992; Sansour and Bufler 1992], and to most of the more recent works cited so far. The problem data and the undeformed configuration with a 4×4 mesh are shown in Figure 15 (owing to symmetry, one quarter of the panel is modeled). Two different thicknesses are examined, with either a coarse mesh of 4×4 curved HSEs or a refined one of 8×8.

The snapping behavior is easily captured by the arc-length procedure. The load-displacement curves, in Figure 16, at the central point A with the 4×4 mesh are plotted and compared with the best results reported in [Sze et al. 2004]; the results with the 8×8 mesh are not included in Figure 16 as they are indistinguishable from those of [Sze et al. 2004]. The thin panel curve (Figure 16a) is traced in 24 steps up to exceed the final load of 3000, with an average of 6.3 iterations per step; the thick panel curve (Figure 16b) is traced in 17 steps, with an average of 5.6 iterations per step. The deformed models

Overall length = 508
Radius = 2540
Overall arc = 0.2 rad
Thickness t = 6.35 or 12.7
Elastic modulus E = 3102.75
Poisson ratio ν = 0.3
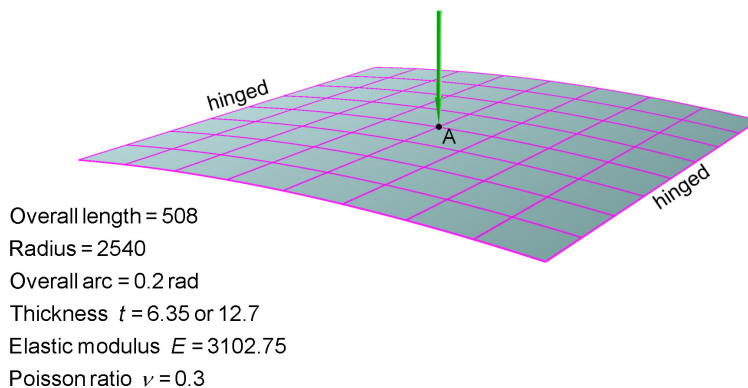
Figure 15. Cylindrical roof under point load: 4×4 mesh in the reference configuration and the applied load.
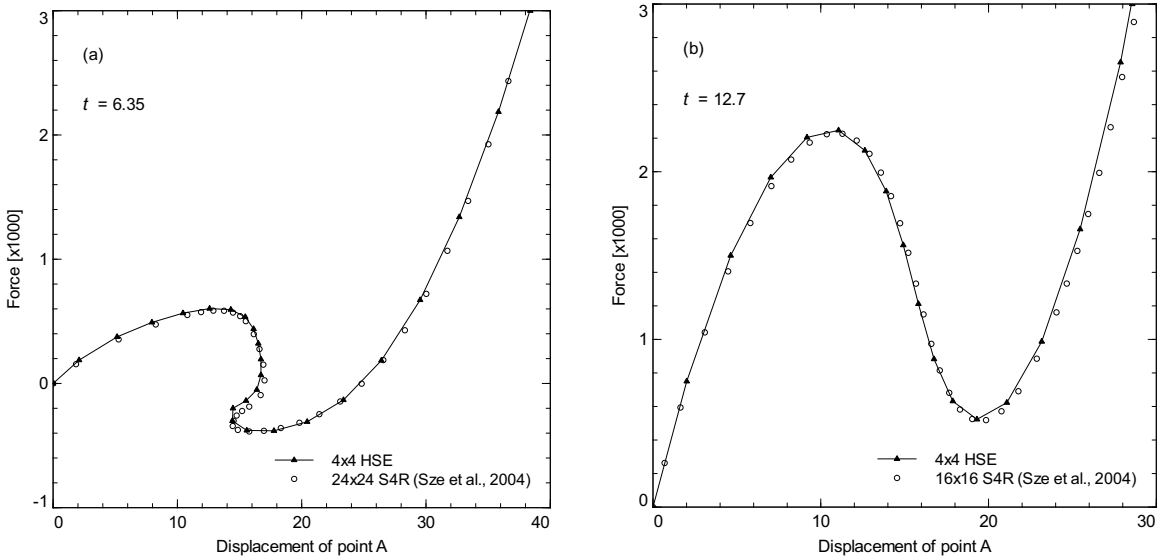
**Figure 16.** Cylindrical roof under point load: load-displacement curves.

$t = 6.35$		$t = 12.7$	
Force	$-w_A$	Force	$-w_A$
188	2.24	750	2.07
375	5.56	1500	4.78
490	8.50	1960	7.22
562	11.02	2191	9.41
586	13.97	2177	12.13
401	16.13	1589	14.91
-65	16.73	566	18.36
-387	16.36	3674	29.97
270	27.15	3000	28.72
3164	38.52		
3000	38.09		

Table 6. Cylindrical roof under point load: displacement of point A with the 8×8 mesh.

are not shown for this test case, as the maximum displacement, despite the strong effect of geometrical nonlinearity, is small and of the order of the panel camber. In Table 6, all the load-displacement pairs from the computations with the 8×8 mesh are listed; during these computations, the arc-length step was allowed to increase, whence the low number of total steps.

4.7. *Cylindrical shell pinched by four radial forces.* The buckling of a cylindrical shell pinched by four radial forces was recently studied [Kuznetsov and Levyakov 2007] to successfully test an unconventional and interesting formulation for a simple curved shell triangle. A short cylindrical shell with free ends is simply supported at four points A on two right-angled diameters, at half the cylinder length. At the

Length $L = 0.1$
Radius $R = 0.1$
Thickness $t = 0.001$
Elastic modulus $E = 0.2 \times 10^{12}$
Poisson ratio $\nu = 0$
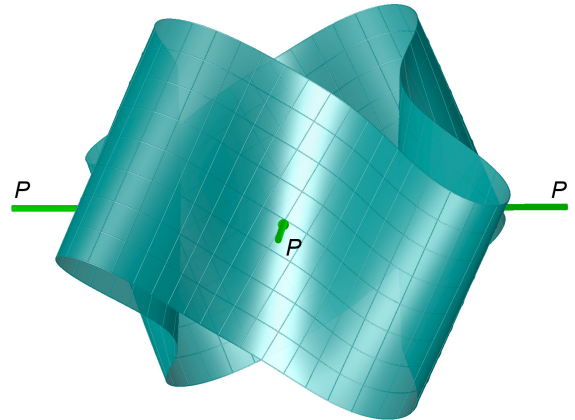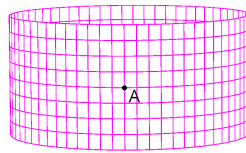
Reference load $P_{\text{ref}} = \dfrac{Et^3}{12(1-\nu^2)} \dfrac{L}{R^2} = \dfrac{500}{3}$

Figure 17. Cylindrical shell pinched by four radial forces: deformed configuration at $P/P_{\text{ref}} = 19.6$ (displacement of point A: $w/R = 0.58$).
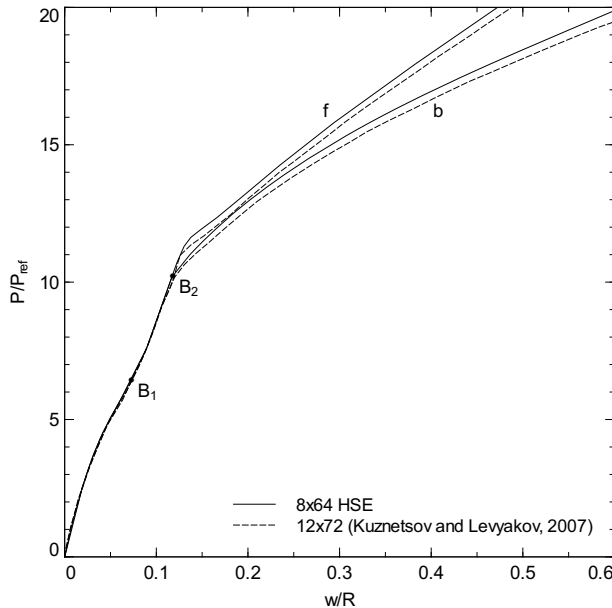
Figure 18. Cylindrical shell pinched by four radial forces: load-displacement curves at points A; fundamental path (f) and branch (b) from the bifurcation point B_2 ($P/P_{\text{ref}} = 10.2$, $w/R = 0.1172$).

constraint points, the shell surface is free to move in the radial direction and to rotate; at the points A themselves, the shell is under the load of four radial forces that push it inward. The problem data and a deformed configuration are shown in Figure 17; the whole shell is modeled with 8×64 curved HSEs.

The problem is solved by the arc-length procedure and yields the load-displacement curves plotted in Figure 18. Along the fundamental path (traced in 17 steps to exceed the target load of $P/P_{\text{ref}} = 20$) the shell deforms with a doubly symmetric four-lobe configuration. As found in [Kuznetsov and Levyakov 2007], buckling occurs at point B_1 on the load-displacement graph, however the deformation keeps the

Fundamental path							
P/P_{ref} 5.705	7.581	10.716	11.301	11.921	13.102	17.941	21.611
w/R 0.0607	0.0893	0.1226	0.1303	0.1488	0.1935	0.3828	0.5422
Bifurcation from B_2							
P/P_{ref} 10.200	11.000	12.000	13.000	13.899	16.045	17.951	20.257
w/R 0.1174	0.1367	0.1672	0.2024	0.2392	0.3463	0.4654	0.6263

Table 7. Cylindrical shell pinched by four radial forces: radial displacements of points A.

four-lobe doubly symmetric. At point B_2, a branch departs from the fundamental path. Along this branch (traced in 33 steps from B_2 to exceed the target load of $P/P_{\text{ref}} = 20$, with 5–6 iterations per step) the shell deforms with a strongly warped configuration, see Figure 17. A fairly good agreement with the published results is observed in Figure 18. Some representative load-displacement pairs are listed in Table 7.

4.8. *Channel-section cantilever.* The buckling of the channel-section cantilever, with the data introduced by [Chróścielewski et al. 1992], has been considered by several authors to test shell elements in folded or intersecting structures, with either elastic or elastoplastic materials, for example, [Ibrahimbegović and Frey 1994; Eberlein and Wriggers 1999; Fontes Valente et al. 2005; Chróścielewski and Witkowski 2006; Klinkel et al. 2008]. In the present test, only the elastic case is considered; the problem data and a postbuckling configuration of the model, made of a regular mesh of $(4 + 12 + 4) \times 36$ HSEs, are shown in Figure 19. Under the transverse force, which is eccentric with respect to the beam elastic axis, the channel twists and at the limit load (116.77 for the present model) the upper flange buckles into longitudinal waves.

Beam length = 36
Web height = 6
Flange width = 2
Thickness = 0.05
Elastic modulus $E = 10 \times 10^6$
Poisson ratio $\nu = 0.333$
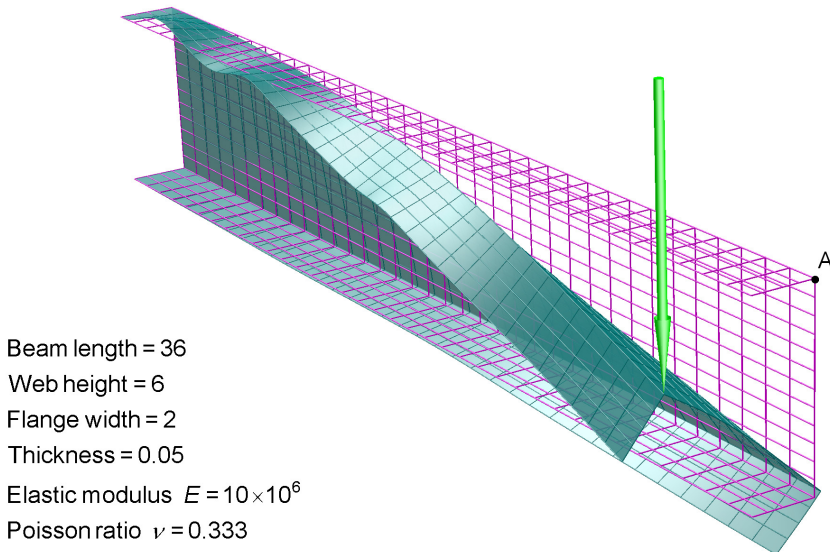
Figure 19. Channel-section cantilever: beam model in the reference configuration and in postbuckling at load of 100.97 (lateral displacement of point A = 4.4524).
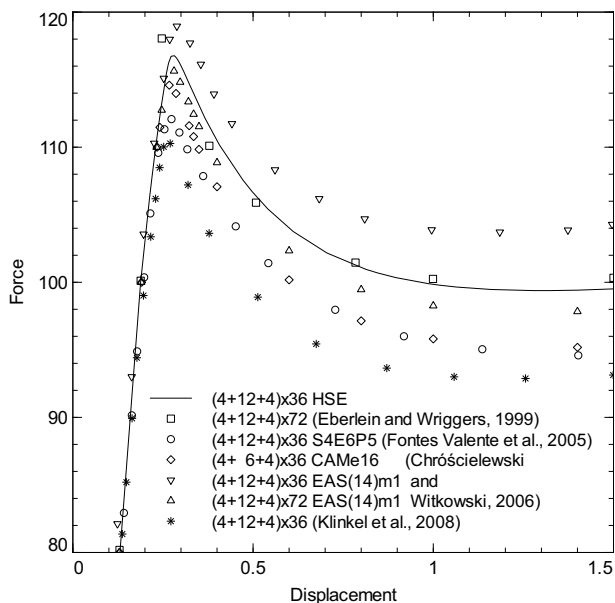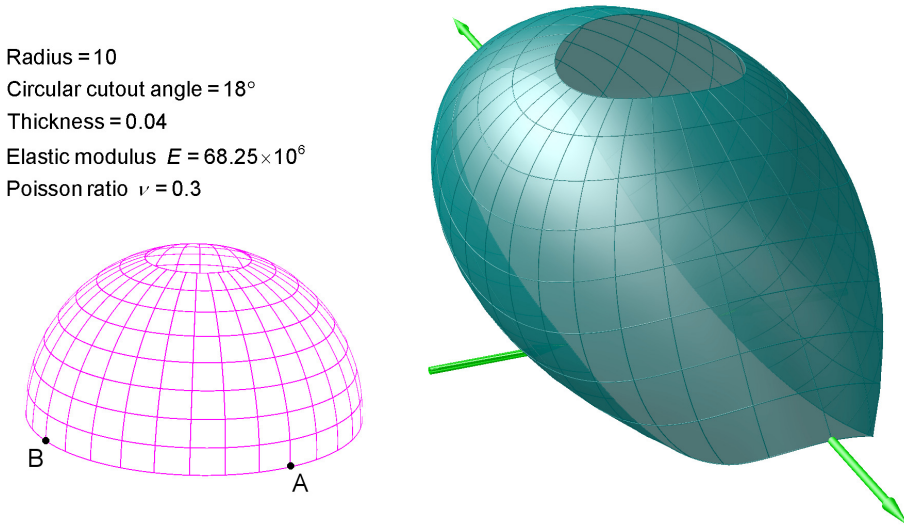
Figure 20. Channel-section cantilever: vertical displacement of point A.

The computation is driven by the monotone Newton–Raphson procedure until a load of 100, then is switched to the arc-length procedure. It takes 36 steps and a total of 190 iterations for the vertical displacement of point A to reach the value 1.5. In Figure 20, a portion of the load-displacement curve is plotted and compared with other curves reported in the literature; the graph is restricted to the load range 80–120 to allow us to distinguish between the curves. Representative displacements are given in Table 8.

Force	Longitudinal	Lateral	Vertical
50.00	0.0077	0.1543	0.0680
100.00	0.0170	0.4411	0.1880
110.78	0.0192	0.5442	0.2336
115.53	0.0201	0.6045	0.2600
116.73	0.0201	0.6427	0.2726
116.70	0.0198	0.6923	0.2847
116.23	0.0192	0.7438	0.2962
114.74	0.0173	0.8606	0.3221
110.18	0.0087	1.2085	0.4063
103.76	−0.0209	1.8799	0.6113
100.96	−0.0561	2.3943	0.8129
99.79	−0.0952	2.8289	1.0173
99.39	−0.1582	3.3735	1.3234
99.83	−0.2408	3.9265	1.6999
100.97	−0.3405	4.4524	2.1295

Table 8. Channel-section cantilever: displacements of point A.

4.9. *Hemispherical shell with a hole.* The hemispherical shell with a polar hole, pinched by four alternating radial forces at the sphere equator, is a very popular benchmark example to test finite element models of doubly curved shells and is included in almost all the papers on nonlinear shell elements. The problem data and a deformed configuration with a rather coarse mesh are shown in Figure 21. Due to symmetry, one quarter of the dome is modeled; several meshes of increasing refinement, from 2×2 to 128×128 doubly curved HSEs, are analyzed.

Radius = 10
Circular cutout angle = 18°
Thickness = 0.04
Elastic modulus $E = 68.25 \times 10^6$
Poisson ratio $\nu = 0.3$

Figure 21. Hemispherical shell with a hole: 8×8 mesh at the final load of 400.
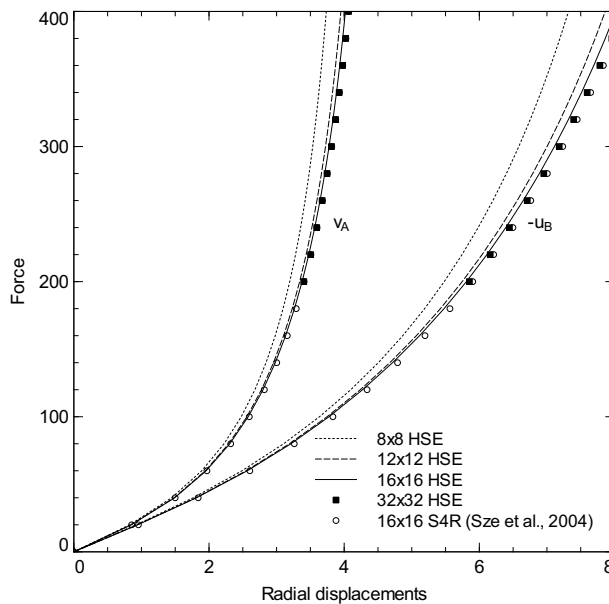
Figure 22. Hemispherical shell with a hole: load-displacement curves.

Force	v_A				$-u_B$			
	8×8	12×12	16×16	32×32	8×8	12×12	16×16	32×32
40	1.447	1.483	1.492	1.498	1.766	1.804	1.816	1.825
80	2.223	2.291	2.308	2.319	3.104	3.190	3.213	3.231
120	2.679	2.776	2.799	2.815	4.098	4.239	4.273	4.299
160	2.980	3.104	3.133	3.154	4.867	5.068	5.116	5.150
200	3.195	3.341	3.377	3.402	5.481	5.746	5.809	5.853
240	3.356	3.522	3.565	3.594	5.983	6.311	6.391	6.445
280	3.481	3.664	3.713	3.747	6.400	6.790	6.888	6.954
320	3.582	3.778	3.834	3.872	6.754	7.199	7.318	7.396
360	3.665	3.873	3.934	3.976	7.057	7.554	7.693	7.784
400	3.735	3.951	4.019	4.065	7.320	7.863	8.023	8.128

Table 9. Hemispherical shell with a hole: radial displacements of points A and B with four different meshes.

The response of the model is measured by the radial displacements of the load-points A and B. The load-displacement curves for four meshes are plotted in Figure 22 and compared with the results published in [Sze et al. 2004]: a good agreement with the reference results is observed. Displacements every 10% of the final force are listed in Table 9. The convergence of the HSE is evident from Figure 23, where the computation with a refined mesh of 128×128 S4R elements by the commercial code ABAQUS is assumed as reference solution.
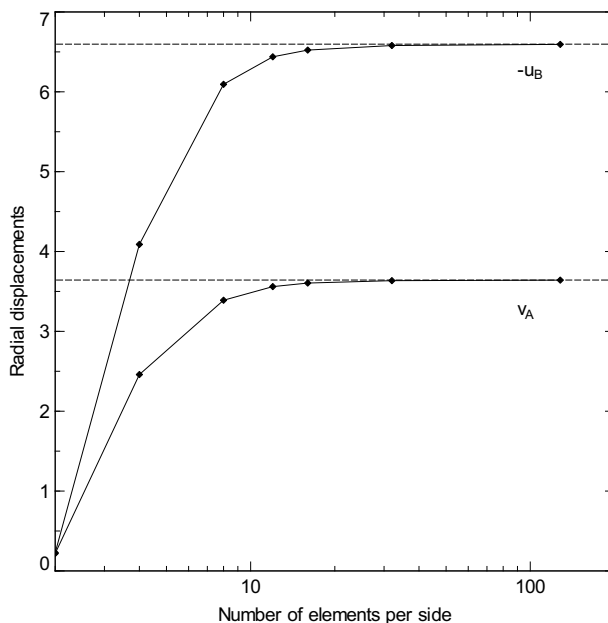
Figure 23. Hemispherical shell with a hole: convergence study at load of 250 (reference values at the dotted lines: $v_A = 3.6426$, $-u_B = 6.5967$).

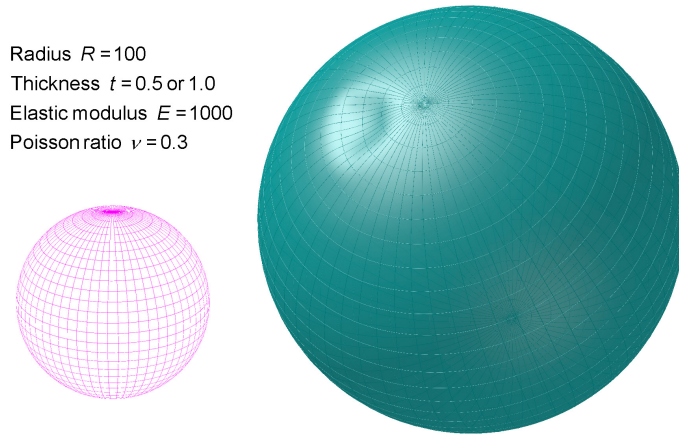| Mesh	Steps	Iterations
8×8	52	325
12×12	57	361
16×16	52	343

Table 10. Hemispherical shell with a hole: number of steps and iterations up to the final load.

The problem is solved by the monotone Newton–Raphson procedure with the automatic step control enabled. To trace the results, load steps of 5% are set by default. Moreover, some computations are repeated by setting a single initial step of 100% to record the number of iterations actually needed to reach the final load (see Table 10); an average of 6–7 iterations per step is observed.

The example of the hemispherical shell is also used to check the significance of the resolution of the nodal mixed variation variables $\eta_{\partial\delta J}$ by (20) and the effectiveness of the contribution to the diagonal term of the tangent matrix from (21). The computation with the 8×8 mesh is repeated after disabling the correction (21). The iterations performed during the loading history are plotted in Figure 24 and compared with the ones of the original computation. When the geometrical nonlinearity becomes important, a remarkable increase in iterations is observed, and a sharp growth is noted when approaching and exceeding the load of 280. After restarting from 280 with the correction enabled again, the final load is reached in a few more steps, yielding exactly the original final displacements, as expected. This test proves the importance of the resolution formulated in (20) in order to provide the correct tangent matrix, capable of following the nonlinear solution process.
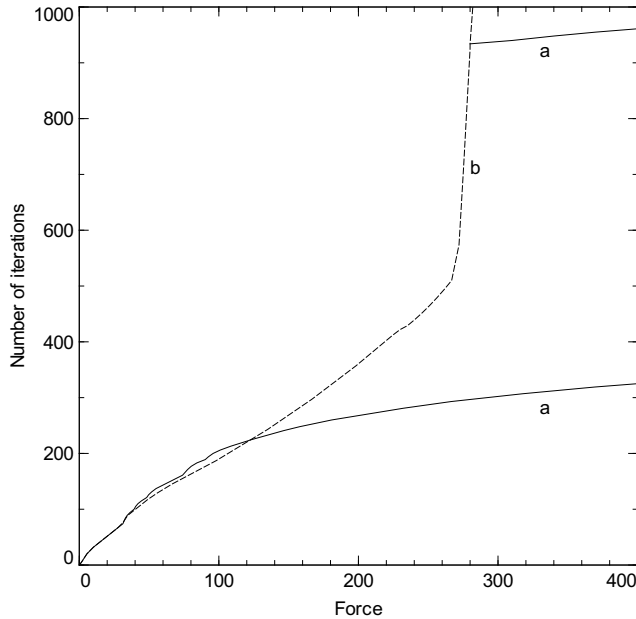
Figure 24. Hemispherical shell with a hole: loading history with 8×8 mesh; comparison between (a) computations with the resolution of the nodal mixed variation variables $\eta_{\partial\delta J}$ and (b) computations without such a resolution.

Radius $R = 100$
Thickness $t = 0.5$ or 1.0
Elastic modulus $E = 1000$
Poisson ratio $\nu = 0.3$

Figure 25. Spherical shell under external pressure: model of case $t = 0.5$ at arc-abscissa 10.594.

4.10. *Spherical shell under external pressure.* The numerical study of the postbuckling behavior of spherical shells under external pressure is one of the most despair-inducing problems in structural mechanics. With no claim made of solving this difficult problem, a sample investigation is presented in this section. The problem data and a postbuckling deformation of the model are shown in Figure 25. The geometric and material properties are taken from [Ricci Maccarini et al. 2001], which modeled only one octant of the sphere, and hence could capture just a limited class of buckling modes. The mesh matches a net of meridians and parallels 6 degrees apart, and consists of 60×30 doubly curved HSEs over the whole sphere. At each pole, the last parallel degenerates into a single point and the relevant nodes to which the quadrilaterals are connected share the same coordinates; the quadrilateral shell elements degenerate into triangles. The pressure is applied as a follower normal-load uniform density at the shell element quadrature points.

Despite the strong deviation of the element geometry from a regular quadrilateral at the poles, the model behaves perfectly. A value of external pressure twice the approximate theoretical critical pressure $p_{\mathrm{ref}} = 2E(t/R)^2/\sqrt{3(1 - \nu^2)}$, predicted by the shallow shell theory, can be reached with the monotone Newton–Raphson procedure in a single step with 4 iterations. This almost linear computation yields a final radial displacement, uniform over the whole shell surface, of 0.4237 with $t = 0.5$ and 0.8473 with $t = 1.0$. To force the shell to buckle, a very small initial imperfection has been assigned by moving randomly the nodes in the radial direction within the range ± 0.001 (that is, $\pm 10^{-5}R$ or $\pm (0.1\text{–}0.2)\% \, t$).

The imperfect spherical shell is analyzed by the arc-length procedure. The solution of case $t = 0.5$ follows the fundamental path till load fraction 1.082 (arc-abscissa $= 3.693$). Then a sudden buckling occurs: the load decreases while a shallow buckle appears. In Figure 26a, the radial displacements of four nodes at latitude $72°$ are plotted against the arc-abscissa. When the arc-abscissa exceeds 7, the pressure stabilizes at a value of about 0.22–0.25 p_{ref} and the role of maximum-displacement holder begins to move from node to node. At the arc-abscissa 10.594 (after 34 steps and 201 total iterations), the node at longitude $126°$ reaches 3.6666, the deepest displacement of the whole analysis; the corresponding buckle is depicted in Figure 25 and its bottom is very close to the observed node. In Figure 26b, the load-displacement curves of the four nodes are plotted. The analysis was pursued further and another peak of load fraction 1.082 was reached; then the load was found to decrease till negative values.
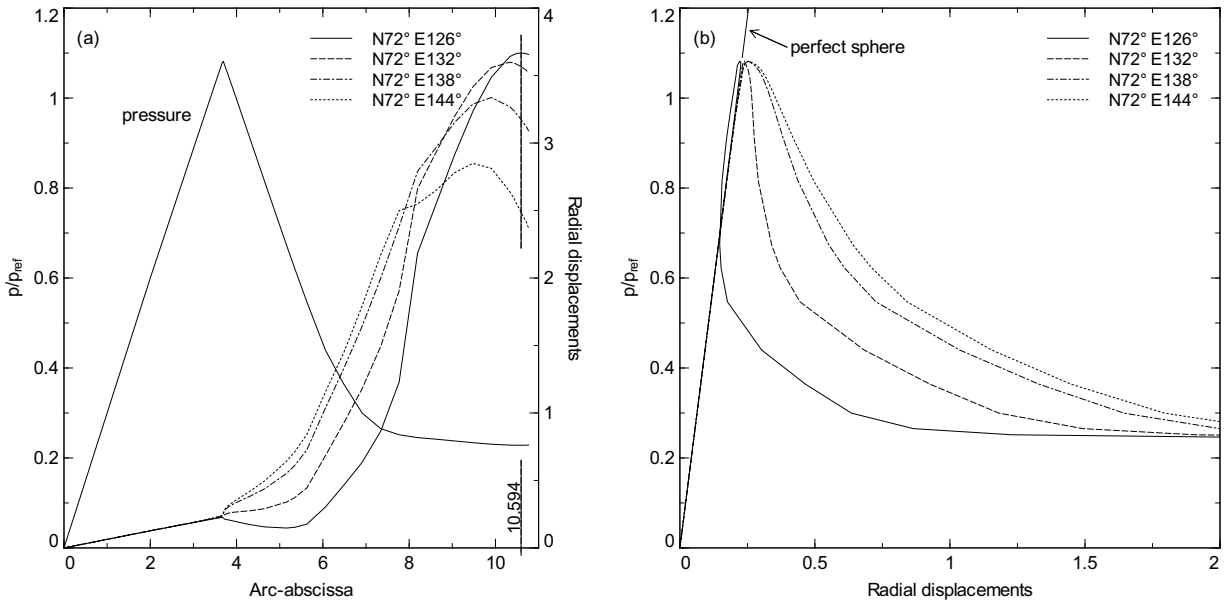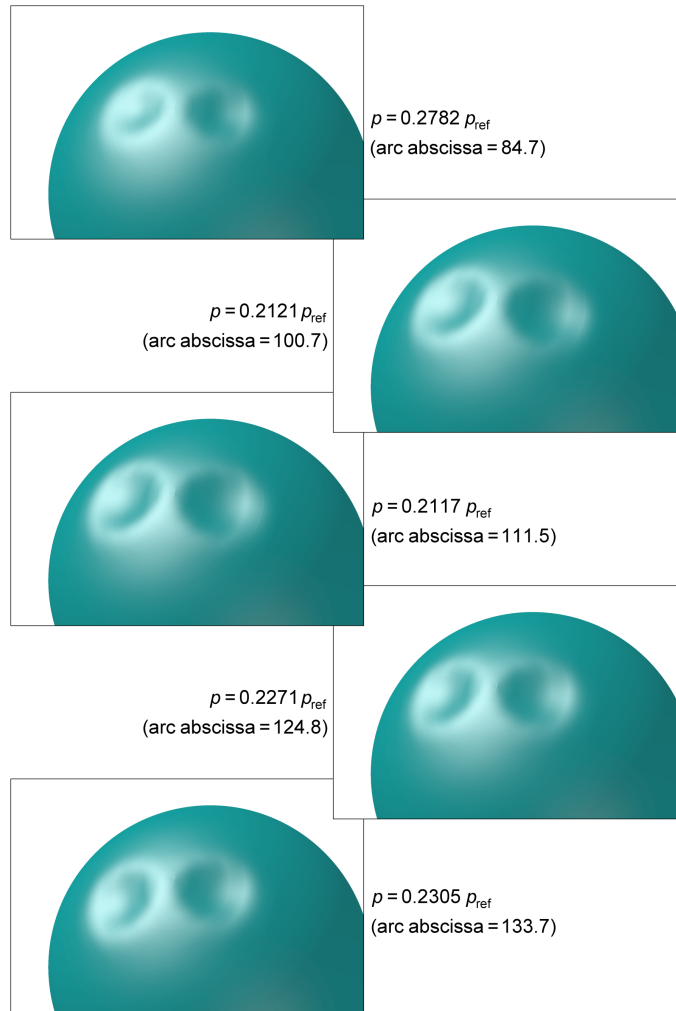
Figure 26. Spherical shell under external pressure (case $t = 0.5$): (a) pressure and four radial displacements against the loading history; (b) load-displacement curves.

With the algorithm of process control at hand, the achievement of a wholly buckled surface as obtained in real experiments is hopeless. In several numerical tests, the occurrence of two or three buckles, either close to each other or far away from each other, was observed. In any case, the buckles manifest a pronounced tendency to migrate, in either a slow or fast manner. As an example, Figure 27 collects five images of the case $t = 1.0$ recorded every 12 load steps: the two buckles keep close to each other and move together on the sphere surface. Also, the repeatability of such computations is questionable: for instance, it is interesting to notice that when assembling the elements concurrently by exploiting the processor multithreading option, analyses starting from identical data never follow exactly the same path when in the postbuckling regime.

5. Conclusion

This paper is focused on computational modeling for nonlinear shell mechanics and is restricted to the simplest case of static boundary value problems involving elastic homogeneous media. Considerations of dynamic problems and anelastic or composite materials are absent and are left as extensions for future work. Nevertheless, the examples and comparisons discussed so far evidence a good performance of the helicoidal shell element (HSE) in several respects. The HSE appears suitable to model in-plane curved and warped shells, thin/thick simply or doubly curved shells with t/R ratios ranging from 2×10^{-3} to 2×10^{-1}, and folded/intersecting shells. It allows a perfect representation of constant-curvature shells, as in the case of the sphere. This quadrilateral shell element is practically insensitive to highly irregular meshes and can easily degenerate into triangles. The HSE has been tested with nonlinear elastic and nearly incompressible materials. In the postbuckling regime, this curving element performs well at the occurrence of snap-through and snap-back conditions. A drawback of the present formulation, already

$p = 0.2782\, p_{\text{ref}}$
(arc abscissa = 84.7)

$p = 0.2121\, p_{\text{ref}}$
(arc abscissa = 100.7)

$p = 0.2117\, p_{\text{ref}}$
(arc abscissa = 111.5)

$p = 0.2271\, p_{\text{ref}}$
(arc abscissa = 124.8)

$p = 0.2305\, p_{\text{ref}}$
(arc abscissa = 133.7)

Figure 27. Spherical shell under external pressure (case $t = 1.0$): sequence of five postbuckling deformations.

pointed out with the solid element [Merlini and Morandini 2005], remains the low step size required to solve certain problems, which is sometimes smaller than the values published in the literature. This undesirable feature of the proposed formulation is of course worthy of further investigation.

It is stressed that the present version of the HSE is essentially a low-order element. For the reader's convenience, a short summary of the element formulation is given here. The integral kinematic field across the thickness is assumed helicoidal and is controlled by the six-parameter dual director $\boldsymbol{\theta}$; the local Biot-axial vector field is assumed linear and is controlled by two stress vectors $\hat{\boldsymbol{\tau}}$ and $\hat{\boldsymbol{\mu}}$ (the constant and linear parts, respectively). From through-the-thickness integration of the linearized internally constrained virtual work functional, and after local condensation of the variables $\boldsymbol{\theta}$ and $\hat{\boldsymbol{\mu}}$, the shell constitutive equations are obtained in incremental form. They are written as functions of twelve components of the material surface dual strains $\boldsymbol{\omega}_\alpha$ and three components of the Biot-axial parameter $\hat{\boldsymbol{\tau}}$. The integration

across the thickness is performed numerically at each surface quadrature point of the shell element domain. The integral kinematic field on the quadrilateral surface is interpolated helicoidally between the orientopositions of four corner-nodes, whereas the Biot-axial parameter is assumed uniform. Integration over the element domain gives the element contributions to the problem residual and tangent matrix. The contributions from external loads and boundary constraints are added directly to the shell surface linearized variational principle.

The numerical tests show that this low-order element is essentially free from locking. A clear description of commonly occurring locking phenomena, such as shear and membrane locking, is given, for example, in [Belytschko et al. 2000], and a careful analysis can be found in [Koschnick et al. 2005]. According to [Bischoff et al. 2004] such phenomena originate from "the inability of a finite element formulation to represent certain deformation modes without unwanted, parasitic strains and/or stresses". In such phenomena, the locking mechanism develops from an improper energy exchange between the involved deformation modes that are badly represented by a poor kinematical approximation. The problem becomes more pronounced when the ratio between the stiffnesses of the flexural deformation modes and the parasitic ones (either transverse shear or membrane modes) decreases — that is, when the thickness diminishes. It can be argued that with classical Euclidean modeling of the continuum, when positions and orientations are uncoupled fields, such improper energy exchanges are more likely to happen than with the proposed helicoidal modeling, where the kinematical representation is consistently built through a unique integral field. It is also general belief that this improper energy exchange is more pronounced the lower the order of the representation is. The helicoidal approximation, both on the through-the-thickness domain with the proposed geometric-invariant model (Part I, Section 4.5) and on the element surface domain with the adopted frame-invariant interpolation (Section 3.2), yields a discrete representation of the kinematic field that proves natural and is able to withstand locking even with low-order interpolants. This is clear from the outstanding representation attainable for thin curved elements with the proposed material surface kinematics; see Figure 1. (Remember that linear interpolants on helicoidal modeling do not mean linear displacement fields, due to the interaction with the nodal rotations.)

References

[Arciniega and Reddy 2007] R. A. Arciniega and J. N. Reddy, "Tensor-based finite element formulation for geometrically nonlinear analysis of shell structures", *Comput. Methods Appl. Mech. Eng.* **196**:4–6 (2007), 1048–1073.

[Areias et al. 2005] P. M. A. Areias, J.-H. Song, and T. Belytschko, "A finite-strain quadrilateral shell element based on discrete Kirchhoff–Love constraints", *Int. J. Numer. Methods Eng.* **64**:9 (2005), 1166–1206.

[Başar et al. 1992] Y. Başar, Y. Ding, and W. B. Krätzig, "Finite-rotation shell elements via mixed formulation", *Comput. Mech.* **10**:3–4 (1992), 289–306.

[Belytschko et al. 2000] T. Belytschko, W. K. Liu, and B. Moran, *Nonlinear finite elements for continua and structures*, Wiley, Chichester, 2000.

[Bischoff and Ramm 1997] M. Bischoff and E. Ramm, "Shear deformable shell elements for large strains and rotations", *Int. J. Numer. Methods Eng.* **40**:23 (1997), 4427–4449.

[Bischoff et al. 2004] M. Bischoff, W. A. Wall, K.-U. Bletzinger, and E. Ramm, "Models and finite elements for thin-walled structures", Chapter 3, pp. 59–137 in *Encyclopedia of computational mechanics, 2: Solids and structures*, edited by E. Stein et al., Wiley, Chichester, 2004.

[Brank 2005] B. Brank, "Nonlinear shell models with seven kinematic parameters", *Comput. Methods Appl. Mech. Eng.* **194**:21–24 (2005), 2336–2362.

[Brank 2008] B. Brank, "Assessment of 4-node EAS-ANS shell elements for large deformation analysis", *Comput. Mech.* **42**:1 (2008), 39–51.

[Brank et al. 2002] B. Brank, J. Korelc, and A. Ibrahimbegović, "Nonlinear shell problem formulation accounting for through-the-thickness stretching and its finite element implementation", *Comput. Struct.* **80**:9–10 (2002), 699–717.

[Büchter et al. 1994] N. Büchter, E. Ramm, and D. Roehl, "Three-dimensional extension of non-linear shell formulation based on the enhanced assumed strain concept", *Int. J. Numer. Methods Eng.* **37**:15 (1994), 2551–2568.

[Bufler 1985] H. Bufler, "The Biot stresses in nonlinear elasticity and the associated generalized variational principles", *Arch. Appl. Mech.* **55**:6 (1985), 450–462.

[Campello et al. 2003] E. M. B. Campello, P. M. Pimenta, and P. Wriggers, "A triangular finite shell element based on a fully nonlinear shell formulation", *Comput. Mech.* **31**:6 (2003), 505–518.

[Cardoso and Yoon 2005] R. P. R. Cardoso and J. W. Yoon, "One point quadrature shell element with through-thickness stretch", *Comput. Methods Appl. Mech. Eng.* **194**:9–11 (2005), 1161–1199.

[Chavan et al. 2007] K. S. Chavan, B. P. Lamichhane, and B. I. Wohlmuth, "Locking-free finite element methods for linear and nonlinear elasticity in 2D and 3D", *Comput. Methods Appl. Mech. Eng.* **196**:41–44 (2007), 4075–4086.

[Chróścielewski and Witkowski 2006] J. Chróścielewski and W. Witkowski, "Four-node semi-EAS element in six-field nonlinear theory of shells", *Int. J. Numer. Methods Eng.* **68**:11 (2006), 1137–1179.

[Chróścielewski et al. 1992] J. Chróścielewski, J. Makowski, and H. Stumpf, "Genuinely resultant shell finite elements accounting for geometric and material non-linearity", *Int. J. Numer. Methods Eng.* **35**:1 (1992), 63–94.

[Eberlein and Wriggers 1999] R. Eberlein and P. Wriggers, "Finite element concepts for finite elastoplastic strains and isotropic stress response in shells: theoretical and computational analysis", *Comput. Methods Appl. Mech. Eng.* **171**:3–4 (1999), 243–279.

[Fontes Valente et al. 2003] R. A. Fontes Valente, R. M. Natal Jorge, R. P. R. Cardoso, J. M. A. César de Sá, and J. J. A. Grácio, "On the use of an enhanced *transverse* shear strain shell element for problems involving large rotations", *Comput. Mech.* **30**:4 (2003), 286–296.

[Fontes Valente et al. 2005] R. A. Fontes Valente, M. P. L. Parente, R. M. Natal Jorge, J. M. A. César de Sá, and J. J. A. Grácio, "Enhanced *transverse* shear strain shell formulation applied to large elasto-plastic deformation problems", *Int. J. Numer. Methods Eng.* **62**:10 (2005), 1360–1398.

[Gruttmann et al. 1992] F. Gruttmann, W. Wagner, and P. Wriggers, "A nonlinear quadrilateral shell element with drilling degrees of freedom", *Arch. Appl. Mech.* **62**:7 (1992), 474–486.

[Hauptmann et al. 2000] R. Hauptmann, K. Schweizerhof, and S. Doll, "Extension of the 'solid-shell' concept for application to large elastic and large elastoplastic deformations", *Int. J. Numer. Methods Eng.* **49**:9 (2000), 1121–1141.

[Ibrahimbegović and Frey 1994] A. Ibrahimbegović and F. Frey, "Stress resultant geometrically nonlinear shell theory with drilling rotations, II: Computational aspects", *Comput. Methods Appl. Mech. Eng.* **118**:3-4 (1994), 285–308.

[Klinkel et al. 2008] S. Klinkel, F. Gruttmann, and W. Wagner, "A mixed shell formulation accounting for thickness strains and finite strain 3D material models", *Int. J. Numer. Methods Eng.* **74**:6 (2008), 945–970.

[Koschnick et al. 2005] F. Koschnick, M. Bischoff, N. Camprubí, and K.-U. Bletzinger, "The discrete strain gap method and membrane locking", *Comput. Methods Appl. Mech. Eng.* **194**:21–24 (2005), 2444–2463.

[Kuznetsov and Levyakov 2007] V. V. Kuznetsov and S. V. Levyakov, "Phenomenological invariant-based finite-element model for geometrically nonlinear analysis of thin shells", *Comput. Methods Appl. Mech. Eng.* **196**:49-52 (2007), 4952–4964.

[Li and Zhan 2000] M. Li and F. Zhan, "The finite deformation theory for beam, plate and shell, V: The shell element with drilling degree of freedom based on Biot strain", *Comput. Methods Appl. Mech. Eng.* **189**:3 (2000), 743–759.

[Merlini 2002] T. Merlini, "Differentiation of rotation and rototranslation", scientific report DIA-SR 02-16, Dipartimento di Ingegneria Aerospaziale, Politecnico di Milano, 2002, Available at http://www.aero.polimi.it/diasr/02-16.pdf.

[Merlini 2003] T. Merlini, "Recursive representation of orthonormal tensors", scientific report DIA-SR 03-02, Dipartimento di Ingegneria Aerospaziale, Politecnico di Milano, 2003, Available at http://www.aero.polimi.it/diasr/03-02.pdf.

[Merlini 2008a] T. Merlini, *Boundary constraint variational formulation for helicoidal modeling*, Aracne, Rome, 2008. Scientific report DIA-SR 08-05.

[Merlini 2008b] T. Merlini, *Variational formulations for the helicoidal modeling of the shell material surface*, Aracne, Rome, 2008. Scientific report DIA-SR 08-06.

[Merlini and Morandini 2004a] T. Merlini and M. Morandini, "The helicoidal modeling in computational finite elasticity, I: Variational formulation", *Int. J. Solids Struct.* **41**:18–19 (2004), 5351–5381.

[Merlini and Morandini 2004b] T. Merlini and M. Morandini, "The helicoidal modeling in computational finite elasticity, II: Multiplicative interpolation", *Int. J. Solids Struct.* **41**:18–19 (2004), 5383–5409. Erratum on *Int. J. Solids Struct.* **42**:3–4 (2005), 1269.

[Merlini and Morandini 2005] T. Merlini and M. Morandini, "The helicoidal modeling in computational finite elasticity, III: Finite element approximation for non-polar media", *Int. J. Solids Struct.* **42**:24–25 (2005), 6475–6513.

[Merlini and Morandini 2008] T. Merlini and M. Morandini, *Material surface elements by the helicoidal shell theory*, Aracne, Rome, 2008. Scientific report DIA-SR 08-08.

[Pimenta et al. 2004] P. M. Pimenta, E. M. B. Campello, and P. Wriggers, "A fully nonlinear multi-parameter shell model with thickness variation and a triangular shell finite element", *Comput. Mech.* **34**:3 (2004), 181–193.

[Reese et al. 2000] S. Reese, P. Wriggers, and B. D. Reddy, "A new locking-free brick element technique for large deformation problems in elasticity", *Comput. Struct.* **75**:3 (2000), 291–304.

[Ricci Maccarini et al. 2001] R. Ricci Maccarini, A. Saetta, and R. Vitaliani, "A non-linear finite element formulation for shells of arbitrary geometry", *Comput. Methods Appl. Mech. Eng.* **190**:37–38 (2001), 4967–4986.

[Sansour and Bednarczyk 1995] C. Sansour and H. Bednarczyk, "The Cosserat surface as a shell model: theory and finite-element formulation", *Comput. Methods Appl. Mech. Eng.* **120**:1–2 (1995), 1–32.

[Sansour and Bufler 1992] C. Sansour and H. Bufler, "An exact finite rotation shell theory, its mixed variational formulation and its finite element implementation", *Int. J. Numer. Methods Eng.* **34**:1 (1992), 73–115.

[Sansour and Kollmann 2000] C. Sansour and F. G. Kollmann, "Families of 4-node and 9-node finite elements for a finite deformation shell theory: an assessment of hybrid stress, hybrid strain and enhanced strain elements", *Comput. Mech.* **24**:6 (2000), 435–447.

[Simo et al. 1990] J. C. Simo, D. D. Fox, and M. S. Rifai, "On a stress resultant geometrically exact shell model, III: Computational aspects of the nonlinear theory", *Comput. Methods Appl. Mech. Eng.* **79**:1 (1990), 21–70.

[Sze et al. 2002] K. Y. Sze, W. K. Chan, and T. H. H. Pian, "An eight-node hybrid-stress solid-shell element for geometric non-linear analysis of elastic shells", *Int. J. Numer. Methods Eng.* **55**:7 (2002), 853–878.

[Sze et al. 2004] K. Y. Sze, X. H. Liu, and S. H. Lo, "Popular benchmark problems for geometric nonlinear analysis of shells", *Finite Elem. Anal. Des.* **40**:11 (2004), 1551–1569.

[Wagner and Gruttmann 2005] W. Wagner and F. Gruttmann, "A robust non-linear mixed hybrid quadrilateral shell element", *Int. J. Numer. Methods Eng.* **64**:5 (2005), 635–666.

[Wriggers and Gruttmann 1993] P. Wriggers and F. Gruttmann, "Thin shells with finite rotations formulated in Biot stresses: theory and finite element formulation", *Int. J. Numer. Methods Eng.* **36**:12 (1993), 2049–2071.

TEODORO MERLINI: teodoro.merlini@polimi.it
Politecnico di Milano, Dipartimento di Ingegneria Aerospaziale, via La Masa 34, 20156 Milano, Italy
http://www.aero.polimi.it/merlini

MARCO MORANDINI: marco.morandini@polimi.it
Politecnico di Milano, Dipartimento di Ingegneria Aerospaziale, via La Masa 34, 20156 Milano, Italy
http://www.aero.polimi.it/morandini/Home

JOURNAL OF MECHANICS OF MATERIALS AND STRUCTURES

jomms.org

Founded by Charles R. Steele and Marie-Louise Steele

Cover design: Alex Scorpan   Cover photo: Wikimedia Commons

See http://jomms.org for submission guidelines.